

# A HUBBLE SPACE TELESCOPE STUDY OF LYMAN LIMIT SYSTEMS: CENSUS AND EVOLUTION<sup>1</sup>

JOSEPH RIBAUDO, NICOLAS LEHNER, J. CHRISTOPHER HOWK  
 Department of Physics, University of Notre Dame, Notre Dame, IN 46556

*Accepted for publication in ApJ*

## ABSTRACT

We present a survey for optically thick Lyman limit absorbers at  $z < 2.6$  using archival *Hubble Space Telescope* observations with the Faint Object Spectrograph and Space Telescope Imaging Spectrograph. We identify 206 Lyman limit systems (LLSs) increasing the number of catalogued LLSs at  $z < 2.6$  by a factor of  $\sim 10$ . We compile a statistical sample of 50  $\tau_{\text{LLS}} \geq 2$  LLSs drawn from 249 QSO sight lines that avoid known targeting biases. The incidence of such LLSs per unit redshift,  $l(z) = dn/dz$ , at these redshifts is well described by a single power law,  $l(z) \propto (1+z)^\gamma$ , with  $\gamma = 1.33 \pm 0.61$  at  $z < 2.6$ , or with  $\gamma = 1.83 \pm 0.21$  over the redshift range  $0.2 \leq z \leq 4.9$ . The incidence of LLSs per absorption distance,  $l(X)$ , decreases by a factor of  $\sim 1.5$  over the  $\sim 0.6$  Gyr from  $z = 4.9$  to  $3.5$ ;  $l(X)$  evolves much more slowly at low redshifts, decreasing by a similar factor over the  $\sim 8$  Gyr from  $z = 2.6$  to  $0.25$ . We show that the column density distribution function,  $f(N_{\text{HI}})$ , at low redshift is not well fitted by a single power law index ( $f(N_{\text{HI}}) \propto N_{\text{HI}}^{-\beta}$ ) over the column density range  $13 \leq \log N_{\text{HI}} \leq 22$  or  $\log N_{\text{HI}} \geq 17.2$ . While low and high redshift  $f(N_{\text{HI}})$  distributions are consistent for  $\log N_{\text{HI}} > 19.0$ , there is some evidence that  $f(N_{\text{HI}})$  evolves with  $z$  for  $\log N_{\text{HI}} \lesssim 17.7$ , possibly due to the evolution of the UV background and galactic feedback. Assuming LLSs are associated with individual galaxies, we show that the physical cross section of the optically thick envelopes of galaxies decreased by a factor of  $\sim 9$  from  $z \sim 5$  to  $2$  and has remained relatively constant since that time. We argue that a significant fraction of the observed population of LLSs arises in the circumgalactic gas of sub- $L_*$  galaxies.

*Subject headings:* Intergalactic Medium — Galaxies: Quasars: Absorption lines

## 1. INTRODUCTION

The absorption features seen in the spectra of QSOs provide a unique opportunity to probe the intergalactic and galactic regions which intersect the lines of sight. In particular, H I absorption studies have allowed us to examine the distribution of gas associated with galaxies, the intergalactic medium (IGM), and the extended gaseous regions of galaxies which serve as an interface to the IGM, over the majority of cosmic time. Often these H I absorbers are placed in three general categories dependent on the H I column density ( $N_{\text{HI}}$ ) of the absorber. The low column density Lyman- $\alpha$  forest absorbers ( $N_{\text{HI}} < 10^{16} \text{ cm}^{-2}$ ) are associated with the diffuse IGM (see review by Rauch 1998). These systems probe low-density, highly ionized gas and are thought to trace the dark matter distribution throughout the IGM (Jena et al. 2005) as well as contain the bulk of the baryons at high redshift (Miralda-Escudé et al. 1996) and a significant amount of the baryons even today (e.g., Penton et al. 2004; Lehner et al. 2007; Danforth & Shull 2008). At the other end, the high column density damped Lyman- $\alpha$  absorbers (DLAs,  $N_{\text{HI}} > 10^{20.3} \text{ cm}^{-2}$ ) appear associated with the main bodies of galaxies (see review by Wolfe (2005), although see Rauch et al. (2009)). These high-density, predominantly neutral systems serve as neutral gas reservoirs for high redshift star formation (Prochaska & Wolfe 2009).

The intermediate column density systems mark the transition from the optically thin Lyman- $\alpha$  forest to the optically thick absorbers found in and around the extended regions of galaxies. Typically these absorbers are easy to identify in QSO spectra due to the characteristic attenuation of QSO flux by the Lyman limit at  $\sim 912 \text{ \AA}$  in the rest frame. These intermediate column density systems are segmented into three additional categories. The low column density absorbers ( $10^{16} \text{ cm}^{-2} \leq N_{\text{HI}} < 10^{17.2} \text{ cm}^{-2}$ ) are known as partial Lyman limit systems (PLLs), the intermediate column density absorbers ( $10^{17.2} \text{ cm}^{-2} \leq N_{\text{HI}} < 10^{19} \text{ cm}^{-2}$ ) are known simply as Lyman limit systems (LLSs, Tytler 1982), and the high column density absorbers ( $10^{19} \text{ cm}^{-2} \leq N_{\text{HI}} < 10^{20.3} \text{ cm}^{-2}$ ) are known as super Lyman limit systems (SLLs, a.k.a. sub-DLAs; O’Meara et al. 2007; Péroux et al. 2002; Kulkarni et al. 2007). These absorbers are the least well-studied and physically understood class of absorbers, especially at  $z \lesssim 2.6$ , i.e. over the past  $\sim 10$  Gyr of cosmic time. The reason for that is because at redshifts  $z \lesssim 2.6$ , the Lyman limit is shifted into the UV, requiring the need for space-based UV observations to observe the Lyman break in spectra.

To date, the majority of spectra used in LLS surveys have been taken from ground-based observations, providing an adequate statistical description of the high redshift ( $z \gtrsim 3.0$ ) absorbers, most recently by Prochaska et al. (2010) and Songaila & Cowie (2010). Previous and recent surveys that partially probe the  $z < 2.6$  regime (Tytler 1982; Sargent et al. 1989; Lanzetta 1991; Storrie-Lombardi et al. 1994; Stengler-Larrea et al. 1995; Songaila & Cowie 2010)

<sup>1</sup> Based on observations made with the NASA/ESA Hubble Space Telescope, obtained at the Space Telescope Science Institute, which is operated by the Association of Universities for Research in Astronomy, Inc. under NASA contract No. NAS5-26555.

have produced samples of tens of LLSs spanning the redshift range  $0 \lesssim z \lesssim 4$ . These surveys studied the statistical nature of LLSs, with some conflicting conclusions as to the evolution of these absorbers over cosmic time. A complete understanding of these optically thick absorbers is crucial as these systems in part determine the strength and shape of the ionizing ultraviolet background (UVB, Shull et al. 1999; Haardt & Madau 1996; Zuo & Phinney 1993). Due to the position of LLS column density with respect to Lyman- $\alpha$  forest systems and DLAs, a priori it is natural to view LLSs as tracing the IGM/galaxy interface. Thus they may provide a potentially unique probe of material moving in and out of galaxies over time. It is for these reasons that the incidence of optically thick absorbers as a function of redshift and the frequency distribution of absorbers as a function of  $N_{\text{HI}}$  serve as a critical parameter in modern cosmological simulations (Rauch 1998; Kereš et al. 2005, 2009; Kereš & Hernquist 2009; Nagamine et al. 2010).

Observations have linked LLSs to the extended regions of galaxies, including their gaseous halos, winds, and the interactions of these with the IGM (e.g., Simcoe et al. 2006; Prochaska et al. 2004, 2006a; Lehner et al. 2009a; Stocke et al. 2010). Simulations have also shown a physical connection between LLSs and galaxies of a wide range of masses at  $z \sim 2$  to 4 (Gardner et al. 2001; Kohler & Gnedin 2007). In addition, surveys of Mg II and C IV absorbers have shown connections to extended galactic environments and indicate the metal absorbers trace similar physical regions as LLSs (e.g., Chen et al. 2001, 2010; Churchill et al. 2000, 2005; Charlton & Churchill 1998; Steidel & Sargent 1992). Mg II absorbers have been studied extensively in optical surveys where the absorbers are observed over the redshift range  $0.3 \leq z \leq 2.2$  and led the way in connecting QSO absorption features with galactic environments (e.g., Tytler 1987; Petitjean & Bergeron 1990; Nestor et al. 2005). Due to the nature of the Mg II absorption lines, which are strong and easily saturated, measurements of the Mg II column density are often impossible. This limits the information available as to their origin, metallicity, and physical properties. LLSs provide a complementary approach in understanding the gas around galaxies and provide a reliable estimate of  $N_{\text{HI}}$  for  $\tau_{\text{LLS}} \leq 2.5$  (from the Lyman limit) and  $\tau_{\text{LLS}} \geq 50$  (from the Lyman- $\alpha$  line) absorbers. For example, measurements of  $N_{\text{HI}}$  allow an examination of the frequency distribution with column density, which provides additional insight into the evolution of the strength and shape of the UVB over cosmic time.

In this work we analyze the population of LLSs at low redshift using a new sample of spectra from archival *Hubble Space Telescope (HST)* observations with the Faint Object Spectrograph (FOS) and the Space Telescope Imaging Spectrograph (STIS). We present the most complete survey to date of LLSs at  $z \leq 2.6$ . We catalogue 206 LLSs at  $z < 2.6$  and examine a redshift path  $\Delta z = 96$  from a statistical sample of 249 QSO spectra to search for  $\tau_{\text{LLS}} \geq 2$  LLSs. We compare our results with previous surveys, including the recent high redshift survey of Prochaska et al. (2010), probing the evolution of LLSs over redshifts  $0 \lesssim z \lesssim 5$ . We connect the observational quantities to physical properties assuming the  $\Lambda\text{CDM}$  cosmology with  $t_0 = 13.47$  Gyr,  $H_0 = 70$

km s $^{-1}$  Mpc $^{-1}$ ,  $\Omega_m = 0.3$ , and  $\Omega_\Lambda = 0.7$  (consistent with WMAP result, Komatsu et al. 2009).

This paper is organized as follows. After a brief description of the properties of LLSs in § 2, we give an overview of the data and the process of assembling the survey sample in § 3. In § 4 we describe the process used to identify LLSs and characterize their properties, while the analysis of these properties, in particular  $l(X)$  and  $f(N_{\text{HI}})$ , is given in § 5. We conclude with a discussion of the connection between galaxies and LLSs in § 6 and a summary of our principal results in § 7.

## 2. DESCRIPTION OF LYMAN LIMIT SYSTEMS

The Lyman limit of neutral hydrogen is located at  $\sim 912$  Å in the rest frame of the absorber. For a background source with intrinsic flux  $F_{\text{QSO}}$  and observed flux  $F_{\text{OBS}}$ , the observed optical depth blueward of the limit is

$$\tau(\lambda \leq \lambda_{\text{LLS}}) = \ln \frac{F_{\text{QSO}}}{F_{\text{OBS}}(\lambda \leq \lambda_{\text{LLS}})}, \quad (1)$$

where  $\lambda_{\text{LLS}}$  is the assigned wavelength of the break in the LLS spectrum. The H I column density of the absorber can then be related to the optical depth using

$$N_{\text{HI}} = \sigma_{\text{HI}}^{-1} \tau_{\text{LLS}} \quad (2)$$

where  $\tau_{\text{LLS}}$  is the optical depth at the Lyman limit of the absorption system and  $\sigma_{\text{HI}} = 6.30 \times 10^{-18} \text{ cm}^2$  is the approximate absorption cross section of a hydrogen atom at the Lyman limit (Spitzer 1978).

It should be noted that while we refer to the absorption systems in this survey as LLSs, a more accurate description would be optically thick absorbers. Since we identify all systems above a minimum  $\tau_{\text{LLS}}$ , we limit our sensitivity to accurately measure large H I column densities. Strong absorbers depress the absorbed flux so low that it cannot be measured. In these cases we have only lower limits for the H I column densities. As a result, some of the absorbers in the sample are likely DLAs or SLLSs, but the lack of coverage of the Lyman- $\alpha$  line prevents us from definitively categorizing these absorbers. Also, the frequency distribution of DLAs and SLLSs is much lower than for standard LLSs, suggesting the strong absorbers comprise a small portion of our sample (see § 5.4).

Due to the different selection criteria in past LLS surveys, we have created two statistical samples of our LLSs. The first sample, R1, defines a LLS as an absorber where  $\tau_{\text{LLS}} \geq 1$ , i.e.,  $N_{\text{HI}} \geq 10^{17.2} \text{ cm}^{-2}$ . The majority of the surveys done through the 1990s were completed using this criterion, although these previous studies were not always rigorous about this restriction. The second sample, R2, defines a standard LLS as an absorber where  $\tau_{\text{LLS}} \geq 2$ , i.e.,  $N_{\text{HI}} \geq 10^{17.5} \text{ cm}^{-2}$ . This second definition is adopted for comparison with the recent high redshift survey by Prochaska et al. (2010).

Although not directly included in our statistical analyses, we have identified many PLLSs with  $\tau_{\text{LLS}} < 1$ , i.e.,  $N_{\text{HI}} < 10^{17.2} \text{ cm}^{-2}$ . These absorbers require a more refined assessment of their selection, and the present sample is incomplete. As a result, we warn against the use of such systems from our sample in statistical analyses. This incompleteness manifests itself in our analysis of the  $f(N_{\text{HI}})$  distribution for LLSs (see § 5.4).

Lastly, in dealing with QSO absorption lines, it is common to exclude absorbers located within an established distance of the background source to eliminate any potential influence the source may have on the number density and ionization state of the systems. We identify these proximate-LLSs as absorbers within  $3000 \text{ km s}^{-1}$  of the background QSO and exclude them from our statistical analyses.

### 3. THE DATA: FOS AND STIS

In this work we make use of archival observations from both the STIS and FOS instruments on board the *HST*. The STIS sample incorporates data from a variety of projects which used the G140L and G230L gratings. These gratings are capable of a resolving power of  $R \sim 1000$ , and wavelength coverages of  $1150 - 1700 \text{ \AA}$  for the G140L and  $1600 - 3100 \text{ \AA}$  for the G230L. All the data were retrieved from the MAST archive and were processed with CALSTIS v2.22 prior to retrieval. Data for objects observed more than once were combined into a single spectrum weighted by the exposure time of the individual spectra. For objects observed with both the G140L and G230L gratings, these data were combined into a single spectrum. Table 1 summarizes the observations used in this work, giving the grating used for an observation, the total exposure time of the observation, and the proposal ID of the observation. Our final analysis of LLS statistics requires careful culling of the data to minimize biases and some of these observations were not included in our final sample; we discuss the criteria used to exclude an observation in § 3.1.

The FOS data can be separated into two distinct portions. First, we use the Bechtold et al. (2002) reductions of observations taken with the G130H, G190H, and G270H gratings.<sup>2</sup> We will refer to this subsample as FOS-H. Data taken with these gratings have a resolving power  $R \sim 1300$ , and wavelength coverages of  $1140 - 1600 \text{ \AA}$  for the G130H,  $1575 - 2330 \text{ \AA}$  for the G190H, and  $2220 - 3300 \text{ \AA}$  for the G270H. We also make use of FOS data using the G160L grating, and we will refer to this subsample as FOS-L. These data have a resolving power  $R \sim 250$  and a wavelength coverage of  $1140 - 2500 \text{ \AA}$ . We treated these data in a manner consistent with the STIS data, with multiple exposures combined to form a single spectrum. Table 2 lists the observations examined for this work, giving the total exposure time of the observation as well as the proposal ID.

For a small number of objects observed with FOS, observations were taken with both the low resolution G160L grating and a combination of the high resolution gratings. In these cases, it is possible to detect a shift in the wavelength array of the G160L spectra relative to the high resolution spectra. For objects where a shift was evident, the G160L spectra were shifted in wavelength space to align with the high resolution data. There were 20 objects where a shift in the wavelength array was detectable, of which the mean shift in spectrum was  $4 \text{ \AA}$ .

The FOS spectra all suffered from background subtraction uncertainties of  $\sim 30\%$  (Keyes et al. 1995) due to the crude nature of the background determination

and lack of scattered light correction in FOS. The error vectors produced by CALFOS do not account for this background uncertainty. For regions strongly absorbed by LLSs, the background uncertainties can dominate the error budget. To estimate this uncertainty, we calculated the background flux as the product of the inverse sensitivity function and the count rate for each grating. Taking  $\sim 30\%$  of this quantity allowed us to account for the error in the initial background subtraction.

#### 3.1. Selection of a Statistical Sample of Absorbers

The initial sample of observations taken from the STIS and FOS archives contained  $\sim 700$  QSOs with redshifts  $0 \lesssim z_{\text{em}} \lesssim 3$  (Tables 1,2; Bechtold et al. 2002). However, not all of these QSOs can be used for LLS studies because the data suffer from a variety of pitfalls (i.e., poor quality or lack of coverage of  $912 \text{ \AA}$  and below in the QSO rest frame) or the selection of the QSO for the STIS or FOS observation is biased in favor or against the presence of a LLS.

To construct a sample of QSO sightlines appropriate for studying LLS statistics we used the following approach. We assigned the redshift of the QSO,  $z_{\text{em}}$ , determined through emission features of the spectrum, using the results from Bechtold et al. (2002) when available and the Veron-Cetty & Veron (2010) QSO database for the remaining objects. We removed from our sample all QSOs with no coverage below  $912 \text{ \AA}$  in the rest frame of the QSO or where the quality of the observation was too poor to establish an estimate for the continuum flux. We also excluded apparent or known broad absorption line QSOs from our sample due to the difficulties in studying intervening absorbers in their spectra. Next we examined the Phase II proposals for each observation to determine if any knowledge of the sight line characteristics were known prior to the execution of the proposal that may represent a bias. For example, QSOs specifically targeted because *International Ultraviolet Explorer* (*IUE*) data indicated the QSO was UV-bright may bias our sample against LLSs. We identified all such potentially biased observations and removed them from our sample. There were also 2 gravitationally lensed QSOs for which we only included one of the pair in our sample, excluding the absorber associated with the lensing galaxy. QSOs targeted because of absorption features known from previous observations, such as Mg II absorption, DLAs, and 21 cm absorption represented the most common selection bias in the present sample. We did not include any LLSs in our statistical sample that were associated with previously identified systems toward these QSOs (these systems are listed in Table 4 with appropriate bias indicators). We did however, include the redshift path covered by these QSOs and any LLSs that occurred at redshifts higher than the targeted absorber redshift. There is a concern that including these observations, in particular the targeted strong Mg II absorbers, may bias our sample against detecting strong H I absorbers along the included redshift path. For the majority of the targeted Mg II observations, additional absorption systems along the line of sight were not accounted for when selecting the QSOs for observation (S. Rao, private communication, 2011). Because of this, we believe there is no significant bias in including the redshift path and non-targeted LLSs of

<sup>2</sup> The data are available through <http://lithops.as.arizona.edu/~jill/QuasarSpectra/>.

these observations. In § 5 we have examined a subset of these observations to show the statistical properties of the observations are consistent with the entire statistical sample. The remaining 249 objects listed in Table 3 comprise our sample.

### 3.2. Survey Redshift Path

To quantify the absorption features found in our sample, we must determine the portion of each spectral observation that is amenable to a robust search. This quantity is referred to as the redshift path of the survey and results from translating the observed spectral wavelengths into redshifts. For our survey we calculated two redshift paths, corresponding to robust searches for LLSs defined as absorbers where  $\tau_{\text{LLS}} \geq 1$  and  $\tau_{\text{LLS}} \geq 2$ . For these two cases, we require the local continuum flux to exceed four times the estimated error array (i.e.  $S/N \gtrsim 4$ ) and to exceed two and a half times the estimated error array (i.e.  $S/N \gtrsim 2.5$ ), respectively. Requiring the  $S/N$  of the observation to be above this threshold allowed us to empirically define an acceptable wavelength range (i.e., redshift path) over which we can reliably detect LLSs. We also require the survey path to end at the redshift  $z_{\text{prox}}$  which corresponds to  $3000 \text{ km s}^{-1}$  blueward of  $z_{\text{em}}$ . The  $S/N$  limits for our redshift path definitions were deduced through the analysis of real and simulated spectra; these limits correspond to our ability to detect  $\tau \geq 1$  or 2 at the 95% confidence level. The second redshift path requirement is an attempt to minimize the effect of the QSO and its environment on the analysis of intervening absorption systems. We note that for objects in our sample, we redefine the quantity  $z_{\text{max}}$  as the lesser value of the maximum redshift that satisfies the  $S/N$  requirement and  $z_{\text{prox}}$ .

In their recent high redshift survey ( $z > 3.5$ ), Prochaska et al. (2010) note several biases that impacted their survey due to the presence of PLLSs. Unidentified PLLSs in their surveys had two main effects, neither of which particularly impacts our survey. In the first, unidentified PLLSs in their spectra could cause the local  $S/N$  to drop below their threshold criterion. These authors calculate the  $S/N$  for comparison against their selection criterion at the wavelength of the QSO Lyman limit and use all of the available path of the observation, unless they are able to identify a PLLS that depresses the  $S/N$  below the threshold at a lower redshift. Thus, not identifying a PLLS could cause them to overestimate the redshift path appropriate for a given QSO. However, we calculate a local  $S/N$  at each point in our spectra and are able to note which regions of a spectrum are unsuitable for use in our survey. Any effect that causes the  $S/N$  to fall below the threshold would shorten the redshift path, even if it were not identified as, e.g., a PLLS. In the second effect discussed by Prochaska et al. (2010), unidentified PLLSs at redshifts just above a higher optical depth absorber caused them to assign a redshift for the latter too high by up to  $\Delta z = 0.1$ . This had the effect of reducing the total redshift path of their survey by a sizable amount, since their typical redshift path per QSO was only  $\Delta z \sim 0.2$ . They estimate this caused overestimates in  $l(z)$  by 30 to 50%. This has a negligible effect on our survey for several reasons. First,  $\sim 90\%$  of the redshifts assigned in our survey come from measurements of Lyman-series lines associated with the LLSs rather

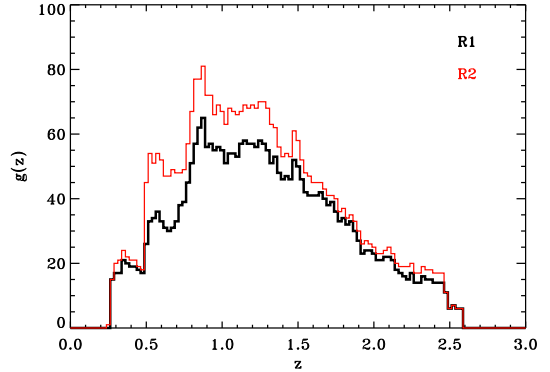


FIG. 1.— The redshift path surveyed with our samples of  $\tau_{\text{LLS}} \geq 1$  (black) and  $\tau_{\text{LLS}} \geq 2$  (red) spectra. The function  $g(z)$  is the number of unique QSOs in our *HST* sample that probe the redshift interval  $\Delta z = 0.025$ , at redshift  $z$ , for LLSs.

than from the break itself. These measurements should be unaffected by the aforementioned bias. Furthermore, the probability of having two overlapping systems, and the resulting impact on the path length calculation, are much smaller at the lower redshifts of our survey. Typically our redshift path per QSO is a factor of  $\sim 4$  larger than the mean of the Prochaska survey, while the number density of absorbers is smaller by a factor of  $\sim 4$ . Even based on these considerations alone, the impact would be mitigated by more than a factor of 10. Furthermore, because the number density of absorbers per unit redshift is significantly lower, the probability of having two in close proximity is also lower by a factor of  $\sim 10$ . Together these diminish the impact of this bias to below a  $\sim 1\%$  effect that only impacts the sight lines without measurements based on Lyman series lines, i.e.,  $< 10\%$  of our sample of LLSs. Altogether, then, these biases play little role in our survey.

Table 3 summarizes the properties of the QSO sight lines that meet these selection criteria. For each object, we give the emission redshift,  $z_{\text{em}}$ , and the maximum and minimum redshifts meeting our redshift path criteria for each optical depth regime,  $z_{\text{max}}$  and  $z_{\text{min}}$ , where  $z_{\text{min}}$  corresponds to the greater value of the minimum redshift that satisfies the  $S/N$  requirement and 20 Å above the minimum wavelength coverage of the observation. We refer to the QSO sightlines in which we can reliably detect a LLS with  $\tau_{\text{LLS}} \geq 1$  as the R1 sample, which contains 229 QSOs and 61 LLSs, while the objects in which we can reliably detect a LLS with  $\tau_{\text{LLS}} \geq 2$  is the R2 sample, which contains 249 QSOs and 50 LLSs.

Figure 1 shows the  $g(z)$  distributions, which represents the number of QSOs with spectral coverage of  $\lambda_{\text{LLS}}$ , as a function of redshift for the R1 and R2 samples. Both samples are most sensitive to the detection of LLSs over the redshifts  $0.8 \leq z \leq 1.5$ . The total integrated redshift path,

$$\Delta z = \int g(z) dz \quad (3)$$

is  $\Delta z(R1) = 79$  and  $\Delta z(R2) = 96$ . Our survey probes a factor of  $\gtrsim 4$  larger redshift path than previous surveys at  $z < 2.6$  ( $\Delta z = 21$ , Jannuzi et al. 1998). Our survey probes a redshift path very similar to the recent high redshift survey of Prochaska et al. (2010), where  $\Delta z = 96$  for LLSs at  $3.3 \leq z \leq 5.0$ .

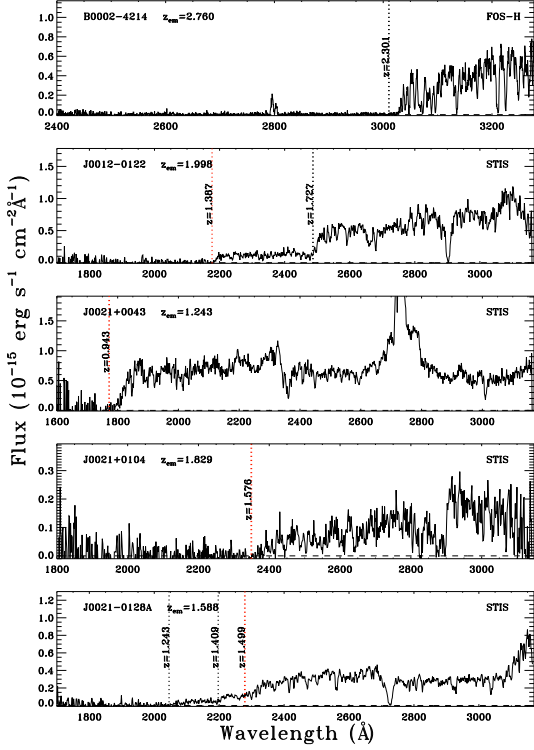


FIG. 2.— The first five observations of the LLSs listed in Table 4. The vertical, dashed lines represent LLSs included in sample R1/R2. The vertical, dashed red lines represent the absorbers that were identified but not included in the statistical analysis for various reasons (see Table 4 for more information). Spectra for each LLS listed in Table 4 can be found in the online version.

#### 4. IDENTIFYING AND CHARACTERIZING LYMAN LIMIT SYSTEMS

We select LLSs on the basis of their Lyman limit absorption (i.e., we do not include absorbers in our statistical sample based only on strong line absorption) for redshifts where the data satisfied our redshift path criteria. The entire list of 206 LLSs found while examining our unabridged sample is given in Table 4. The absorbers used in the statistical analysis are designated with R1 or R2. There are 61 LLSs in the R1 sample and 50 LLSs in the R2 sample. A sample of the spectra for the observations can be found in Figure 2, where each QSO spectrum is plotted with a vertical dashed line at the location of an established H I absorber. The red dashed lines indicate systems which were identified but not included in our statistical analysis. The complete sample of LLSs identified in this work are available in the online version of Figure 2.

In general, as seen in Figure 2, the break produced by a  $\tau_{\text{LLS}} \geq 1$  LLS is abrupt enough to be found in even low S/N ( $\sim 4$ ) and resolution spectra. However, as we discussed above the occasional presence of PLLSs can complicate the situation. In particular, assigning the continuum flux level redward of the Lyman break can become difficult. To minimize the potential error associated with this effect, we adopt a two-step process. First we use an automated search to identify potential Lyman limits. This automated search was checked by-eye and found to highlight absorbers with  $\tau \geq 1$  quite well. These methods allowed us to identify absorbers where

$\tau < 1$ , but we stress the sample of PLLSs detected is not complete. Subsequently we use an interactive routine to fit the continuum flux, the optical depth of the system, and the characteristic continuum recovery blueward of a Lyman limit (see below). While our statistical sample contains only LLSs that satisfy our  $\tau_{\text{LLS}} \geq 1$  or  $\tau_{\text{LLS}} \geq 2$  criteria, we have attempted to identify every optically thick and partially optically thick absorber present in our spectra. This is important for accurate continuum fitting and provides a sample of PLLSs that we use in the analysis of the  $f(N_{\text{HI}})$  distribution presented in § 5.4.

We adopted the composite QSO spectrum developed by Zheng et al. (1997) as a general model of the QSO continuum. We scaled the continuum to each QSO spectrum over a relatively absorption free wavelength range of the spectrum. We found the majority of QSO observations were fitted well by this composite. We then used a running chi-square tool to identify portions of the spectrum where the QSO spectrum deviated from the composite. For each pixel in the spectrum, a running  $\chi^2$  goodness of fit parameter was calculated comparing the fitted continuum with the observed spectrum over  $\sim 30 \text{ Å}$ .<sup>3</sup> This largely excluded false identifications due to strong absorption lines present throughout the spectrum. Spectra not well fitted by this routine were individually examined for the possibility of a Lyman break, although the number of such spectra is very small.

Once a spectrum was flagged as containing a possible LLS, the spectrum was examined more thoroughly to identify the redshift of the break and any Lyman series lines present. When possible, the Lyman series lines were used to determine the redshift of the absorber. However, if the Lyman limit was located near the maximum wavelength of the spectrum or the resolution of a spectrum was too low to identify individual absorption lines (i.e. the majority of FOS-L observations) we used the Lyman break to set the redshift. We define the redshift of a LLS determined from the break as

$$z_{\text{LLS}} = \frac{\lambda_{\text{LLS}}}{912 \text{ Å}} - 1, \quad (4)$$

where  $\lambda_{\text{LLS}}$  is the wavelength of the observed Lyman break. In Table 4, we list  $z_{\text{LLS}}$  from our analysis. The typical statistical error on the redshift determination from the Lyman series lines is  $\sigma_z = 0.001$  for the FOS-H and STIS spectra. The statistical errors on  $z_{\text{LLS}}$  are larger when using the break, about 0.010 for the FOS-H and STIS spectra and 0.014 for the FOS-L spectra. As we used two different methods to determine  $z_{\text{LLS}}$ , possible systematics may be introduced. We tested this by using LLSs for which the redshift could be determined from both the Lyman lines and break. We found a systematic shift of 0.007 in the redshifts determined from the break in the FOS-H and STIS spectra, but not for the FOS-L (possibly because the resolution is far cruder). For the few redshifts of the LLS determined from the Lyman break in the FOS-H and STIS spectra, we systematically corrected  $z_{\text{LLS}}$  by the 0.007 shift.

<sup>3</sup> At low redshift the attenuation of the QSO flux blueward of 912 Å (in the rest frame of the QSO) due to intervening Lyman- $\alpha$  lines is quite small compared to high redshift. This allowed us to model the QSO flux with the composite spectrum quite well over all wavelengths, including regions which probed the lower redshift Lyman- $\alpha$  forest.

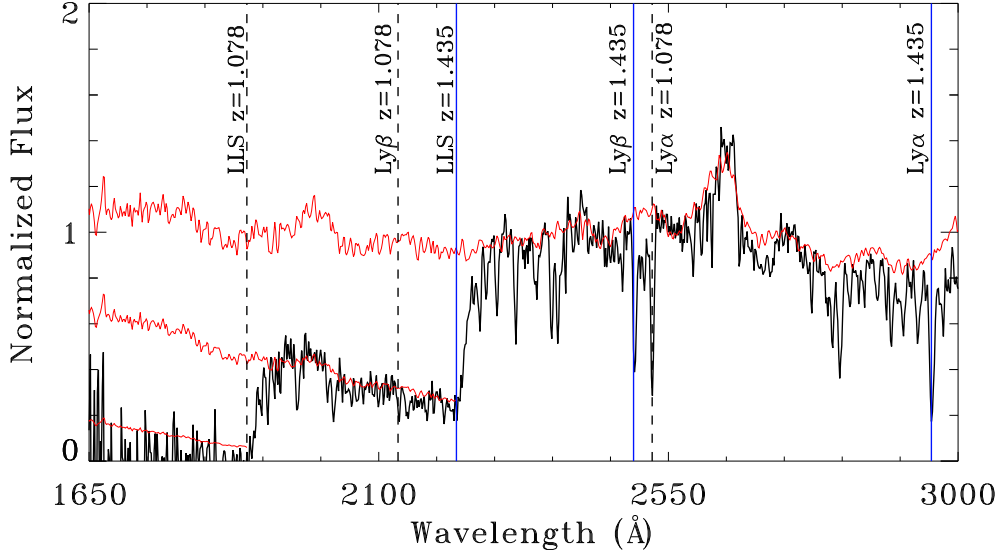


FIG. 3.— The spectrum of J1322+4739 with a composite spectrum overplotted (in red). The Lyman limit at  $z = 1.435$  ( $\tau = 1.27 \pm 0.04$ ) is identified with blue lines. Blueward of the limit, the composite is overplotted again with the characteristic recovery of the flux. The Lyman limit at  $z = 1.078$  ( $\tau > 2.44$ ) is identified with the dashed black lines. This is a snapshot of the plots produced using our method to identify LLSs and characterize their properties.

Once a redshift is assigned, we measure the optical depth at the Lyman limit for each absorber. We interactively refined the fit of the composite QSO continuum model to each spectrum. We determine the optical depth at the limit by comparing the continuum flux,  $F_{\text{QSO}}$ , with the observed (absorbed) flux,  $F_{\text{OBS}}$ , as in Equation 1. For many PLLSs and a few LLSs, the residual flux below the limit is sufficient to satisfy our  $S/N$  selection criteria for further LLS searches at  $z < z_{\text{LLS}}$  of the highest redshift system. We derive a continuum blueward of the highest redshift LLS in a spectrum by modeling the recovery of the flux due to the wavelength dependence of the optical depth. The continuum flux in the recovery region,  $F_{\text{REC}}$ , is

$$F_{\text{REC}} = F_{\text{QSO}} e^{-\tau_{\text{LLS}} \left( \frac{\lambda}{912\text{\AA}} \right)^3}, \text{ for } \lambda < 912\text{\AA}. \quad (5)$$

Once  $F_{\text{REC}}$  is defined, we repeat our LLS search for systems at redshifts below the initial system after renormalizing our best fit continuum fit according to Equation 5. Figure 3 shows the method of fitting the continuum onto a QSO spectrum, identifying a LLS, and modeling the recovery of the spectrum blueward of a Lyman limit.

For absorption systems where the residual absorbed flux blueward of the break was determined to the  $3\sigma$  level, we report optical depth measurements with accompanying errors. For systems where we could not detect the residual absorbed flux to the  $3\sigma$  level, we treat the optical depth measurement as a lower limit and report the  $2\sigma$  lower limit. The optical depth measurements can be found in Table 4, where  $N_{\text{HI}}$  is also reported.

## 5. STATISTICAL ANALYSIS AND RESULTS

In this section we present the results of our survey. The first subsection examines the redshift density of LLSs and how the results from sample R1 and R2 compare to past studies of LLSs. The following subsections introduce a  $\Lambda$ CDM cosmology to connect the statistical treatment of our samples to physical structures throughout the uni-

verse such as the mean separation of LLSs, the incidence of LLSs as a function of absorption distance, and the column density distribution function. In each subsection, we first generalize the analysis, as to make it applicable to both of our samples. Following the general treatment, the individual samples are explored and discussed when appropriate.

### 5.1. The Redshift Density of Intervening LLSs

The redshift density of LLSs,  $l(z)$ ,<sup>4</sup> is a statistical quantity that is directly related to the QSO observations. The standard method for estimating  $l(z)$  is to simply calculate the ratio of the number of LLSs,  $N$ , detected in a redshift interval to the total survey path,  $\Delta z$  (defined in Equation 3), contained in that redshift interval:

$$l(z) = \frac{N}{\Delta z}. \quad (6)$$

Figure 4 presents the values of  $l(z)$  for both samples, R1 and R2. We first estimated  $l(z)$  in redshift intervals where the binning was arbitrarily selected to provide approximately the same number of LLSs in each interval. Table 5 lists the properties of these redshift intervals for the R1 and R2 samples. Following previous work (e.g. Tytler 1982), we model the redshift evolution in  $l(z)$  as a power law of the form:

$$l(z) = l_* \left( \frac{1+z}{1+z_*} \right)^\gamma. \quad (7)$$

This functional form was originally chosen when the Einstein-de Sitter models were the preferred cosmologies. At the time, evolution in the LLS distribution was found if  $\gamma \neq 1$  for  $q_0 = 0$  or  $\gamma \neq 0.5$  for  $q_0 = 0.5$ . We use this functional form for the historical significance and the usefulness it provides in comparing our results with previous

<sup>4</sup> This quantity has often been denoted in the past by a variety of symbols including  $N(z)$ ,  $n(z)$ , and  $dN/dz$ .

surveys, but we note there is no physical or a priori reason to expect a particular functional form. However, the power law fit does do a reasonable job fitting the  $l(z)$  distribution.

Using the maximum-likelihood method (e.g. Tytler 1982; Sargent et al. 1989), a best-fit estimate for  $\gamma$ , and from that  $l_*$ , can be determined for both samples. For the R1 sample ( $\tau_{\text{LLS}} \geq 1$ ) we find  $\gamma = 1.19 \pm 0.56$  and  $l_* = 0.85$ . For sample R2 ( $\tau_{\text{LLS}} \geq 2$ ) we find  $\gamma = 1.33 \pm 0.61$  and  $l_* = 0.59$ . For both samples we adopt  $z_* = 1.5$ , which corresponds to  $\langle z_{\text{LLS}} \rangle = 1.5$  and can be chosen arbitrarily. These best-fit models are overplotted on the  $l(z)$  data in Figure 4.

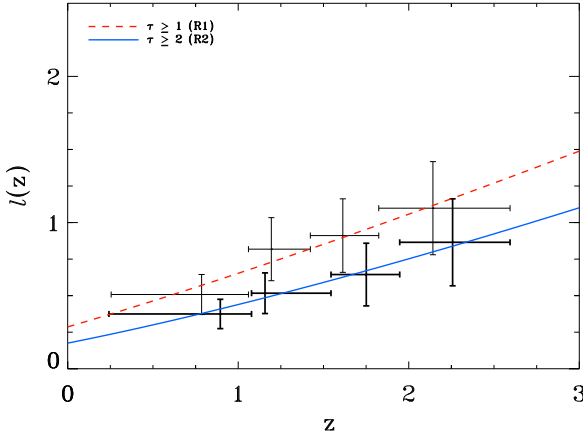


FIG. 4.— The evolution of the redshift density,  $l(z)$ . The values for  $l(z)$  can be found in Table 5. From a maximum-likelihood analysis, the best fit power law:  $l(z) = l_*[(1+z)/(1+z_*)]^\gamma$ , with  $z_* = 1.5$ , is  $l_* = 0.85$  and  $\gamma = 1.19 \pm 0.56$  (for  $\tau_{\text{LLS}} \geq 1$ ) and  $l_* = 0.59$  and  $\gamma = 1.33 \pm 0.61$  (for  $\tau_{\text{LLS}} \geq 2$ ).

To check if the difference between the observed distribution and the adopted power law expression is statistically significant, we test the null hypothesis, that the observed and predicted cumulative distributions of LLSs with redshift are distinct, using a Kolmogorov-Smirnov test. The KS test yields a minimum probability of  $P=0.95$  that we can reject the null hypothesis, using the entire redshift range encompassed by both the low and high redshift samples. Thus there is a strong probability that we can reject this null hypothesis.

As mentioned in § 3.1, we examined the potential biases associated with including redshift paths toward QSOs with targeted strong Mg II absorbers, which constitute a significant fraction of our statistical sample ( $\sim 25\%$ ). To empirically test for any bias, we separately analyzed the statistical properties of these observations and compared their properties with the statistical properties of the total sample. From the STIS observations of Rao et al. (PID 9382 & 8569), we composed a sample of 79 QSO observations. This sample contained 17 (16)  $\tau \geq 1$  (2) LLSs over a redshift path of  $\Delta z = 22.65$  (28.01), giving  $l(z) = 0.75 \pm 0.20$  ( $0.57 \pm 0.14$ ). These values are well within  $1\sigma$  of the  $l(z)$  for the full sample ( $0.77 \pm 0.11$  and  $0.52 \pm 0.08$  for  $\tau \geq 1$  and 2, respectively; Table 5). As a further check, we then separately analyzed the remaining 170 QSO observations to compare with the statistical properties of the total sample. This sample contained 44 (34)  $\tau \geq 1$  (2) LLSs over a redshift path of  $\Delta z = 56.57$  (68.13), giving  $l(z) = 0.78 \pm 0.13$

( $0.49 \pm 0.09$ ), which again is well within the  $1\sigma$  values for the full sample (Table 5). This suggests any biases associated with these observations have a negligible impact on our analysis and results.

Over the past 30 years, there have been a variety of LLS surveys (Tytler 1982; Sargent et al. 1989; Lanzetta 1991; Storrie-Lombardi et al. 1994; Stengler-Larrea et al. 1995; Jannuzi et al. 1998; Prochaska et al. 2010; Songaila & Cowie 2010), and, as a result, a variety of estimates of  $l(z)$ . Many of these previous surveys examined large redshift intervals (typically spanning  $0 \lesssim z \lesssim 4$ ) but have largely been statistically dominated by high redshift ( $z \gtrsim 2.5$ ) LLSs. It is due to this inhomogeneity, combined with the lack of low redshift LLSs, that there is uncertainty as to the true statistical distribution of LLSs over the redshift range  $0 \lesssim z \lesssim 4$ . Lanzetta (1991) was the first to argue for a potential break in the evolution of the redshift density of LLSs at  $z \sim 2.5$ , where he found the low redshift ( $z < 2.5$ ) LLSs showed relatively constant  $l(z)$  and the high redshift ( $z > 2.5$ ) LLSs showed a rapidly evolving  $l(z)$ . However, both Storrie-Lombardi et al. (1994) and Stengler-Larrea et al. (1995) argued, based on samples spanning the redshift range  $0 \lesssim z \lesssim 4$ , that the  $l(z)$  for LLSs is best described as moderately evolving over the entire range and fit by a single power law in  $(1+z)$ . Figure 5 presents  $l(z)$  values from the R1 sample, as well as the  $l(z)$  fits from these previous surveys (with the parameters listed in Table 6). These previous surveys used a  $\tau_{\text{LLS}} \geq 1$  criterion for inclusion in the sample, but it is not clear this was applied in a uniform manner (Stengler-Larrea et al. 1995). Our results for  $l(z)$  over  $0.25 \leq z \leq 2.6$  are consistent with the surveys of Storrie-Lombardi et al. (1994) and Stengler-Larrea et al. (1995), both of which fit  $l(z)$  over the redshift range  $0 \lesssim z \lesssim 4$ .

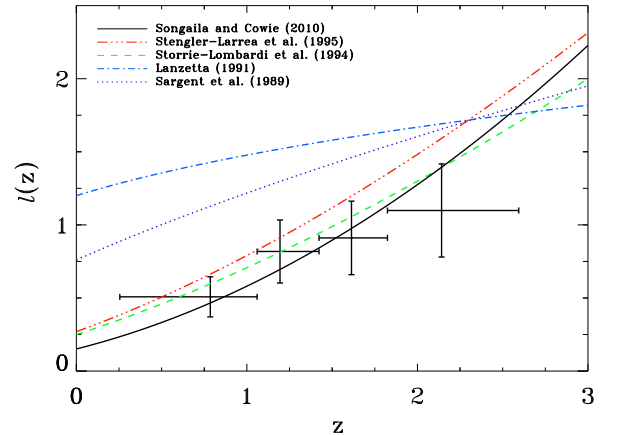


FIG. 5.— Estimates for the functional form of  $l(z)$  from previous studies of  $\tau_{\text{LLS}} \geq 1$  LLSs plotted on top of our R1 sample. The fits are parameterized as power laws with individual parameters listed in Table 6. Our results are consistent with the results of Stengler-Larrea et al. (1995) and Storrie-Lombardi et al. (1994), studies which probed the range  $0 < z < 4$ .

Recently, Prochaska et al. (2010) released a survey of high redshift LLSs (with  $\tau_{\text{LLS}} \geq 2$ ) using the SDSS-DR7 that samples a redshift range ( $3.5 \leq z \leq 4.4$ ) that does not overlap our survey redshifts. They find the  $l(z)$  for high redshift LLSs can be described as rapidly evolv-

ing over the range  $3.5 \leq z \leq 4.4$ . Our model of  $l(z)$  is inconsistent with the Prochaska et al. (2010) survey when extrapolated to  $z > 3$ , as the Prochaska results are inconsistent with ours if extrapolated to  $z < 2.6$ . It was a similar disagreement seen in the high and low redshift samples of the Lanzetta (1991) work that led to the argument for a break in the power law description of  $l(z)$  for LLSs. To investigate the possibility and significance of a broken power law fit to the redshift density of LLSs, we combine the recent high redshift sample from Prochaska et al. (2010) with our low redshift sample to examine the statistical nature of LLSs from  $0 \lesssim z \lesssim 5$ .

We refer to the combined R2 and Prochaska et al. (2010) samples as the RP10 sample. This combined sample of *HST* and SDSS observations contains 685 QSOs and 206 LLSs with  $\tau_{\text{LLS}} \geq 2$ . The total redshift path probed in RP10 is  $\Delta z = 172$ . This redshift path is a factor of  $\sim 2$  greater than the recent LLS survey from Songaila & Cowie (2010), which spanned redshifts up to  $z \sim 6$ . In Figure 6, we present our estimate for  $l(z)$  over this expanded redshift range. We find  $l(z)$  from the combined sample can be described by a single power law (Equation 7) with  $\gamma = 1.83 \pm 0.21$  and  $l_* = 1.62$ , for  $z_* = 3.23$ . Table 7 lists the properties of the  $l(z)$  bins used for display purposes in Figure 6 and the values associated with each bin. To confirm the observations are well modeled by a single power law, a KS test was applied to the cumulative distribution function of observed and predicted LLSs (see Figure 6). The KS test yields a probability of at least  $P = 0.95$  that the null hypothesis, the observed and predicted distributions represent different distributions, can be discarded. Thus the RP10 sample supports the conclusions of Storrie-Lombardi et al. (1994), Stengler-Larrea et al. (1995), and more recently Songaila & Cowie (2010), that a single power law is sufficient to describe  $l(z)$  over  $0 < z < 5$ .

It should be noted that in the original analysis of the SDSS-DR7 sample, Prochaska et al. (2010) limited the redshift path to  $z \leq 4.4$ . This was done because the inclusion of  $z > 4.4$  into their sample appeared to produce an artificially low  $l(z)$  result for  $4.4 < z < 5.0$ , which they argued was unlikely to be physical. We include this extra redshift path from their sample, under the reasoning that arbitrary binning of the data for display purposes can produce artificial departures from a trend that in no way affects the statistical analysis of the maximum likelihood method. In our redefined bins, the artificial drop apparent at  $z > 4.4$  is no longer present. To insure the extra redshift path is not solely responsible for our ability to fit the combined sample with a single power law, we conducted our analysis on the combined *HST*/SDSS for both situations ( $z_{\text{max}} \leq 4.4$  and unrestricted  $z_{\text{max}}$ ) and found both conditions produce single power law fits that are consistent and good describers of the data. It is also interesting to note that if  $z_{\text{max}}$  is unrestricted for the SDSS sample alone, the best fit curve for the high redshift sample is described by  $\gamma = 2.79 \pm 1.46$  and  $l_* = 1.94$ . This description of  $l(z)$  for the high redshift LLSs presents a less convincing argument for the need of a break in the power law, because the difference in power law indices between low and high redshift is less extreme.

Our analysis indicates that it is not necessary to introduce a broken power law to model the statistical evolution of the redshift density of LLSs over  $0 \lesssim z \lesssim 5$ .

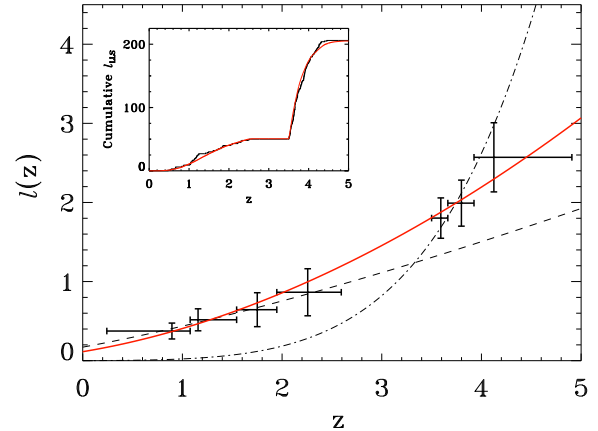


FIG. 6.— The incidence of LLSs per redshift,  $l(z)$ , for the combined SDSS-DR7 and R2 samples (RP10,  $\tau \geq 2$ ). The single power law:  $l(z) = l_*[(1+z)/(1+z_*)]^\gamma$ , with  $z_* = 3.23$ , is  $l_* = 1.62$  and  $\gamma = 1.83 \pm 0.21$ , is plotted with the  $l(z)$  values taken from Table 7. To check the statistical significance of the single power law, a KS test was administered to the sample. The cumulative distribution function for the observations overplotted with the predicted distribution from our best fit power law can be found in the insert. The KS test gives a probability  $P = 0.95$  that we can reject the null-hypothesis that the two distributions originate from different populations. The dashed and dot-dashed curves are the power law fits derived for the low and high redshift samples respectively.

However, we stress a sample with coverage of the  $2.5 \lesssim z \lesssim 3.5$  region will be needed to truly rule out a break (J. O'Meara et al. in prep.). We note that the redshift density is really an observational statistic, and the difference between a single or broken power law may not carry much significance over to the physical quantities with which it is related. In § 5.2, § 5.3, and § 5.4 we put these results into the context of a cosmology and discuss the implications for the evolution and nature of LLSs to  $z \sim 5$ .

## 5.2. The Incidence of LLSs per Absorption Distance

The number of LLSs per absorption length,  $l(X)$  (Bahcall & Peebles 1969), is defined as

$$l(X)dX = l(z)dz \quad (8)$$

where

$$dX = \frac{H_0}{H(z)}(1+z)^2dz, \quad (9)$$

and

$$H(z) = H_0(\Omega_\Lambda + \Omega_m(1+z)^3)^{1/2}. \quad (10)$$

The quantity  $l(X)$  is defined such that it is constant if the product of the comoving number density of structures giving rise to LLSs,  $n_{\text{LLS}}$ , and the average physical cross section of the structure,  $\sigma_{\text{LLS}}$ , is constant, i.e.,  $l(X) \propto n_{\text{LLS}}\sigma_{\text{LLS}}$ .

Figure 7 shows the quantity  $l(X)$  plotted as a function of fractional lookback time for the RP10 sample ( $\tau_{\text{LLS}} \geq 2$ ). We see that  $l(X)$  experiences a rapid decrease for  $\sim 0.6$  Gyr corresponding to a decrease in redshift from  $z = 4.9$  to  $3.5$ . After this rapid drop,  $l(X)$  decreased slowly over  $\sim 8$  Gyr, from  $z = 2.6$  to  $0.25$  (See Table 7). The results in Table 7 show that  $l(X)$  fell by a factor of  $\sim 1.5$  over  $\sim 0.6$  Gyr at high redshift and by another factor of  $1.5$  over  $\sim 8$  Gyr at low redshift.

Figure 7 demonstrates why differing results are found regarding the broken (or not) power laws in the statistical treatment of the redshift density of LLSs. The dashed red line and dotted blue line in the plot are the best fit power laws for  $l(z)$  (transformed into  $l(X)$  using Equation 8 and 9) for our low redshift sample and the high redshift sample of Prochaska et al. (2010). The solid black line is the best fit power law to the RP10 sample (again transformed into  $l(X)$  using Equation 8 and 9). The nature of power laws makes it difficult to extrapolate a fit based on observations in only the low or high redshift regime (in the regime where the power law is derived, the fit is nearly linear, making it extremely difficult to match observations in a regime outside of where it was derived). It is only when the observations are combined that we are able to produce a consistent single power law. We have mentioned the need for a study of the intermediate redshift regime ( $2.5 \leq z \leq 3.5$ , J. O’Meara et al. in prep.), which will allow for a more definitive assessment of the absorber distribution.

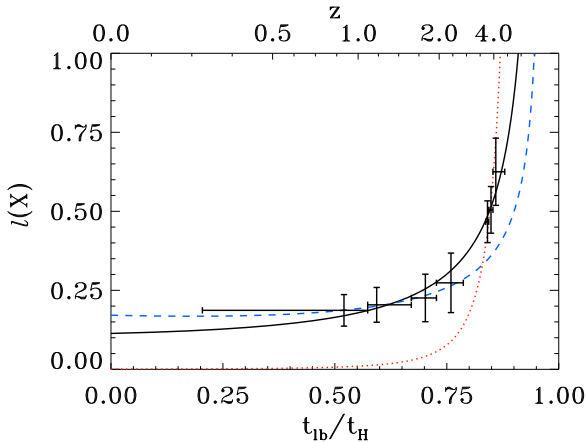


FIG. 7.— The incidence of LLSs per absorption distance,  $l(X)$ , plotted as a function of fractional look-back time. The values for  $l(X)$  can be found in Table 7. The solid line is the power law result for the maximum-likelihood analysis on the RP10 sample ( $\tau \geq 2$ ). The dashed blue line and the dotted red line are the power law fits from the R2 sample and high redshift sample from (Prochaska et al. 2010). This figure illustrates the problems that arise when attempting to fit the high and low redshift regimes with power law fits derived in either the high or low redshift only.

As previously stated, the behavior in  $l(X)$  is related to the comoving number density of LLSs as well as the physical size of the absorbers. This rapid decrease in  $l(X)$  over a short timescale at high redshift indicates either the physical size of LLSs has decreased substantially in this time or the comoving number density of LLSs has dropped significantly. A moderate decrease in both properties could also give rise to this behavior, but as we will show in § 6, when we associate LLSs with galaxies we find the physical size of LLSs must undergo significant evolution from  $z \sim 5$  to 2.

### 5.3. The Mean Proper Separation of LLSs

The number density of optically thick absorbers throughout the Universe determines the mean free path of hydrogen ionizing photons, and in turn, sets the shape and intensity of the UVB. We can calculate an upper limit to this mfp using  $l(X)$  of  $\tau_{\text{LLS}} \geq 2$  absorbers, as

calculated in § 5.2. It is only an upper limit because we have not included the  $\tau_{\text{LLS}} < 2$  absorbers that contribute to the overall absorption of hydrogen ionizing photons. Using  $l(X)$ , we can calculate the average proper distance,  $\Delta r_{\text{LLS}}$ , a photon travels before encountering a  $\tau_{\text{LLS}} \geq 2$  LLS (e.g., Prochaska et al. 2010) as

$$\Delta r_{\text{LLS}} = \frac{c}{H_0} \frac{1}{(1+z)^3 l(X)}. \quad (11)$$

With the RP10 sample we find that  $\Delta r_{\text{LLS}}$  varies from  $\sim 50 - 3700 h_70^{-1}$  Mpc proper distance from  $z \sim 5$  to 0.3 (Table 7, also note  $\Delta r_{\text{LLS}}$  was calculated for R1 and R2 in Table 5). In Figure 8  $\Delta r_{\text{LLS}}$  is shown as a function of redshift (data points and red curve), along with the mean free path of hydrogen ionizing photons (black curve) estimated by Faucher-Giguère et al. (2009) (It should be noted that while the calculation of the mean free path by Faucher-Giguère et al. (2009) is dependent on an assumed H I distribution, their estimated mean free path is in agreement with the mean free path calculation from Prochaska et al. (2009)). The shaded region emphasizes the difference between the two curves, which can be associated with the contribution from PLLSs and  $\tau_{\text{LLS}} < 2$  LLSs that were not included in this calculation. We note the ratio between the distance a photon travels before encountering a  $\tau_{\text{LLS}} \geq 2$  LLS and the mean free path of a hydrogen ionizing photon is increasing with decreasing redshift. Consider the extreme redshifts of the plot; at  $z \sim 5$ ,  $\Delta r_{\text{LLS}}$  is a factor of  $\sim 1.5$  larger than the predicted mean free path, while at  $z \sim 0$ ,  $\Delta r_{\text{LLS}}$  is a factor of  $\sim 3.5$  larger than the predicted mean free path. Assuming a mean free path consistent with Faucher-Giguère et al. (2009), this suggests that the  $\tau_{\text{LLS}} < 2$  hydrogen absorption systems have become increasingly more important for absorption of Lyman continuum photons as the universe has evolved.

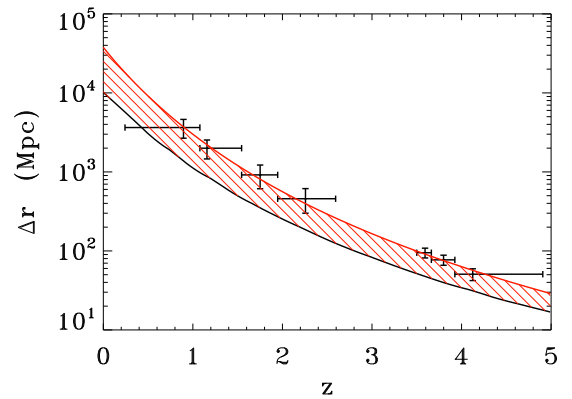


FIG. 8.— The average proper distance a photon travels before encountering a  $\tau \geq 2$  LLS, plotted as a function of redshift. The data points correspond to values taken from Table 7, with the solid red line representing the interpolated functional form for  $\Delta r_{\text{LLS}}$ . We have included in this plot the mean free path of a hydrogen ionizing photon (solid black line), taken from the recent work on the ionizing background spectrum by Faucher-Giguere et al. (2009). The shaded region highlights the difference in the two curves, which corresponds to the effect PLLSs and  $\tau_{\text{LLS}} < 2$  LLSs (which were not included in our RP10 statistical sample) have on the opacity of the universe.

#### 5.4. The Differential Column Density Distribution Function

In this subsection, we combine our low redshift sample with previous works on the low- $z$  ( $z \lesssim 2.6$ ) IGM to place constraints on the differential column density distribution  $f(N_{\text{HI}})$  over 10 orders of magnitude in  $N_{\text{HI}}$ . This distribution is defined such that  $f(N_{\text{HI}}, X)dXdN_{\text{HI}}$  is the number of absorption systems with column density between  $N_{\text{HI}}$  and  $N_{\text{HI}} + dN_{\text{HI}}$  and redshift path between  $X$  and  $X + dX$  (e.g., Tytler 1987),

$$f(N_{\text{HI}})dN_{\text{HI}}dX = \frac{m}{\Delta N_{\text{HI}}\Sigma\Delta X}dN_{\text{HI}}dX, \quad (12)$$

where  $m$  is the observed number of absorption systems in a column density range  $\Delta N_{\text{HI}}$  centered on  $N_{\text{HI}}$  and  $\Sigma\Delta X$  is the total absorption distance covered by the spectra. The first moment of the distribution is also the incidence of absorbers per absorption distance,  $l(X) = \int_{N_1}^{N_2} f(N)dN$ . Empirically, it has been shown that at low and high redshift,  $f(N_{\text{HI}})$  may be fitted by a power law for various  $N_{\text{HI}}$  regimes (e.g., Tytler 1987; Rao et al. 2006; Lehner et al. 2007; O’Meara et al. 2007):

$$f(N_{\text{HI}})dN_{\text{HI}}dX = C_{\text{HI}}N_{\text{HI}}^{-\beta}dN_{\text{HI}}dX. \quad (13)$$

The slope,  $\beta$ , may vary with the considered  $z$  or  $N_{\text{HI}}$  intervals, and, as discussed below and elsewhere (e.g., Wolfe et al. 2005; Prochaska & Wolfe 2009), the functional form can be more complicated than a single power law, especially when the entire observed  $N_{\text{HI}}$  range is considered. In Figure 9, we show the  $f(N_{\text{HI}})$  column density distribution at  $z \lesssim 2.6$ . The data and analyses for different  $N_{\text{HI}}$  regimes come from various origins that we detail below. In the studies where another cosmology was chosen to calculate  $\Delta X$  (Lehner et al. 2007; Williger et al. 2010), we have updated the cosmology to that used in the present study (see Equation 9). At  $z < 1.65$ , the DLA sample was selected based on known strong Mg II–Fe II systems (Rao et al. 2006). Their sample consist principally of data similar to those presented in this work (but rejected from our sample of LLSs because they were specifically targeted) with the addition of *IUE* spectra. Owing to their selection criteria, the sample has selection biases (Rao et al. 2006; Prochaska & Wolfe 2009), although Rao et al. (2006) argued that they are relatively well understood and dealt with (in the DLA regime). Rao et al. (2006) found that their DLA ( $\log N_{\text{HI}} \geq 20.3$ ) sample could be fitted with  $\beta = 1.4$  (represented by the solid red line in Figure 9). The dot-dashed cyan curve shows a fit assuming the power law index for the DLA at high redshift with  $\beta = 1.8$  ( $20.3 \lesssim \log N_{\text{HI}} \lesssim 21.8$ ) (Prochaska et al. 2010), which seems to provide a reasonable fit to the DLA measurements for  $z < 1.65$  as well. The similar slope of  $f(N_{\text{HI}})$  at both high and low  $z$  is consistent with a non-evolution of  $f(N_{\text{HI}})$  for the DLA as argued by Prochaska & Wolfe (2009).

At the other end of the  $N_{\text{HI}}$  spectrum,  $\log N_{\text{HI}} \lesssim 16$ —the Lyman- $\alpha$  forest regime, we consider two complementary samples that probe  $z < 0.5$  (Lehner et al. 2007) and  $0.5 < z < 2.0$  (Janknecht et al. 2006). We also complement the lower redshift interval with the 3C 273 sightline analyzed by Williger et al. (2010). At  $z < 0.5$ , the data come from the high resolution STIS E140M echelle

mode while at higher redshift the data come from STIS E230M as well as VLT/UVES and Keck/HIRES data. The H I column densities (and Doppler parameters) were derived by fitting the Lyman- $\alpha$  line (and higher Lyman series lines if present) thanks to the high resolution of these spectra. This method works well for systems with  $\log N_{\text{HI}} \lesssim 15.5$  if several Lyman series lines are used (e.g., Lehner et al. 2006) or with  $\log N_{\text{HI}} \lesssim 14$  (depending on the  $b$ -value) if only the Lyman- $\alpha$  transition is used. For the  $z < 0.5$  sample, several Lyman series lines were used when possible. For the higher redshift sample, Janknecht et al. (2006) also used different atomic transitions to constrain the Doppler parameter. We note that their sample include a few PLLSs and LLSs, but the H I column densities of these systems often have errors in excess of 1 dex. We excluded those systems from our analysis. Using the maximum-likelihood method, we first fitted the two Lyman- $\alpha$  forest samples separately, finding no difference between these two redshift regimes. We therefore combined both samples and fitted them simultaneously. We find  $\beta = 1.72 \pm 0.02$  and  $\log C_{\text{HI}} = 11.14$  in the  $\log N_{\text{HI}}$  interval [13.2, 14.5] (which is shown by the blue line in Figure 9). Changing the upper bound by +2 dex and the lower bound by +0.5 dex gives consistent results (within  $\lesssim 1\sigma$ ). However, changing the lower bound by  $-0.1$  dex decreases  $\beta$  by  $-0.05$  (more than  $2\sigma$ ), and  $\beta$  drops even more if the lower bound decreases further. As indicated in Figure 9, there is a turnover in the distribution at  $\log N_{\text{HI}} \simeq 13.2$ , which is likely due to the incompleteness of the sample at these column densities.<sup>5</sup> While the slope derived for Lyman- $\alpha$  forest is very similar to that predicted in recent cosmological simulations (Davé et al. 2010), the observations do not indicate an evolution of  $\beta$  in this redshift regime, as inferred in the simulations.

Finally, the column density distributions of the PLLSs, LLSs, and SLLSs ( $19 \leq \log N_{\text{HI}} < 20.3$ ) have so far remained largely uncategorized at  $z \leq 2.6$ . For the SLLSs,  $\tau_{\text{LLS}}$  is far too large to estimate  $N_{\text{HI}}$  from the Lyman break, but in this regime, the amount of H I is large enough that the Lyman- $\alpha$  transition produces damping wing from which  $N_{\text{HI}}$  can be estimated. In our sample, Lyman- $\alpha$  is covered in just 7 sightlines when  $\tau_{\text{LLS}} > 3.5$ . In two of these cases, there is no detection of Lyman- $\alpha$ , but the data were obtained from the low resolution FOS observations. In the other five cases, Lyman- $\alpha$  is observed, but in four of them, the equivalent width implies column densities around  $10^{19} \text{ cm}^{-2}$  or less. As the spectral resolution of the data is low and line contamination is likely, we relied on other recent works to constrain  $f(N_{\text{HI}})$  in the SLLS regime. Specifically, we use the surveys of O’Meara et al. (2007) and Péroux et al. (2003), which include 16 SLLS at  $1.7 < z < 2.6$ , overlapping the high redshift portion of our LLS sample and the

<sup>5</sup> Janknecht et al. (2006) typically found  $\beta \simeq 1.60$ –1.64, but they set a completeness for their sample at  $\log N_{\text{HI}} = 12.9$ . Setting the lower bound to 12.9 dex, we found  $\beta = 1.61$ , a value very similar to theirs and substantially smaller than  $\beta = 1.72 \pm 0.02$ . Their completeness value was not justified, and based on our analysis a lower limit of 13.2 dex appears more appropriate. The signal-to-noise in 9 of the 11 sight lines (depending on the wavelength) indeed is not dissimilar from the lower redshift sample, where Lehner et al. (2007) showed that the completeness was 13.2 dex based on an analysis of the column density distribution.

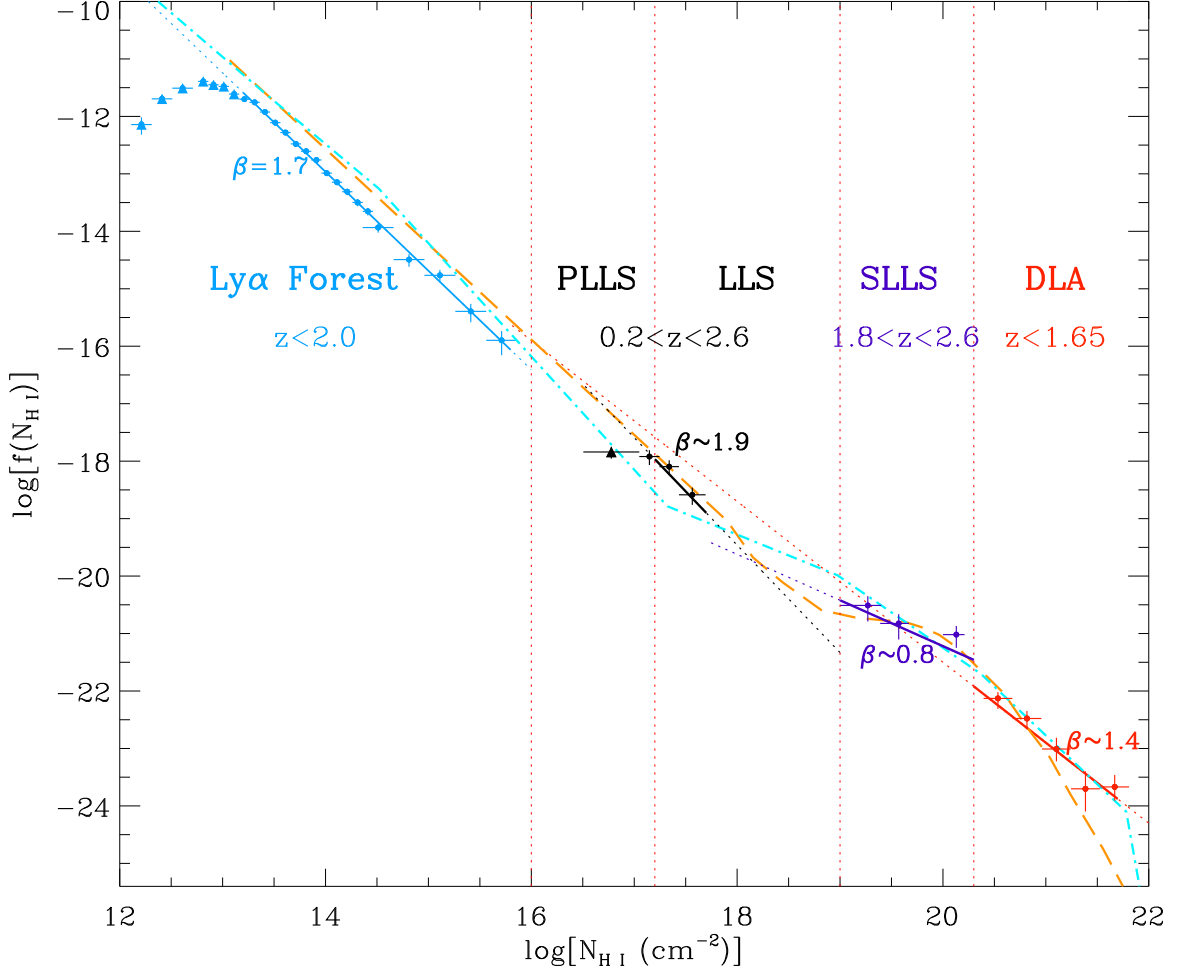


FIG. 9.— The differential density distribution ( $f(N_{\text{HI}})$ ) is plotted against  $\log N_{\text{HI}}$ . The data are shown with filled circles or triangles and error bars. The triangles indicate that the sample is incomplete at these column densities. The blue, black, violet, and red solid curves are maximum-likelihood fits to the Lyman- $\alpha$  forest, LLS, SLLS, and DLA samples. The solid part of these lines shows the  $N_{\text{HI}}$  portion where the fit was undertaken, and the dotted part is the extension in other  $N_{\text{HI}}$  regimes. The dot-dashed cyan curve is the estimation of  $f(N_{\text{HI}})$  at  $z \sim 3.7$  by Prochaska et al. (2010, the solid black curve in their Figure 14; bear in mind that for  $14.5 \leq \log N_{\text{HI}} < 19$ ,  $f(N_{\text{HI}})$  is quite uncertain). The orange long-dashed curve is a model from Corbelli & Bandiera (2002) at low  $z$  where  $f(N_{\text{HI}})$  is assumed to follow a single power law, but  $f(N_{\text{HI}})$  deviates from a single power law as a result of photoionization by the UV background (see §5.4 for more details).

Lyman- $\alpha$  forest samples.<sup>6</sup> We estimate the total absorption path probed for the SLLS searches to be  $\Delta X \simeq 107$  ( $\Delta X \simeq 29$  for the Péroux et al. sample, and  $\Delta X \simeq 78$  for the O’Meara et al. sample). The bins for display of the data were chosen so there are  $\sim 5$  systems per bin (see Figure 9). For the PLLSs and LLSs, we considered our sample of QSO sightlines, where we reject sight lines having LLSs with only limits on the optical depth (and hence on  $N_{\text{HI}}$ ). The main effect of the removal of the limits is to increase slightly the normalization of the fit by  $\sim 0.1$  dex. This is too small a difference to have any impact on our result and should not impact the power law slope. This reduces our sample to 50 systems and a total absorption path  $\Delta X = 156$ . In Figure 9 we show the adopted bins for  $16.5 \leq \log N_{\text{HI}} \leq 17.8$ . The first bin corresponds to optical depths in the intervals  $[0.2, 0.7]$ , i.e. where our sample is incomplete; we treat this bin as a lower limit.

<sup>6</sup> Péroux et al. (2005) subsequently produced a second survey of SLLS, but their redshift coverage mostly targeted higher redshifts with a negligible redshift path at  $z < 2.6$ .

We used the maximum-likelihood method to fit the data with a power law distribution in  $f(N_{\text{HI}})$  (Equation 13). Our first attempt was to fit the LLS and SLLS simultaneously, but no adequate fit was found with a single slope  $\beta$ . We, therefore, fitted the LLS and SLLS separately. For the SLLS, we find  $\beta = 0.8^{+0.3}_{-0.1}$  for  $19.1 \leq \log N_{\text{HI}} \leq 20.2$  (where the upper and lower bounds were allowed to vary by  $\pm 0.1$  dex to estimate the errors). For LLS, we derived  $\beta \approx 1.9 \pm 0.3$  for  $17.2 \leq \log N_{\text{HI}} \leq 17.7$  (as the  $N_{\text{HI}}$  interval spans only 0.5 dex, changing the upper and lower bounds by  $\pm 0.1$  dex led to an unstable fit; we consider this result as tentative). We note that if we integrate  $f(N_{\text{HI}})$  in the intervals  $\log N_{\text{HI}} = [17.3, 18.2]$  and  $\log N_{\text{HI}} = [18.2, 20.2]$ , with the respective  $\beta$  functional forms (where we assume that each is correct to the point where they intersect at  $\sim 18.2$  dex, see Figure 9), we find  $l(X) \sim 0.5$ , which is not too dissimilar from the results presented in Table 5 that gives  $l(X) \simeq 0.3$ , providing some independent support to our results. It is evident that more data are needed in the PLLS and the LLS/SLLS regimes to better discern the

true shape of  $f(N_{\text{HI}})$  in these  $N_{\text{HI}}$  intervals. However, our analysis suggests that there must be an inflection point in  $f(N_{\text{HI}})$  in the LLS regime, and, likely, a second inflection point in order to connect the PLLS to the Lyman- $\alpha$  forest systems. We note that the  $\beta = 1.7$  slope distribution fits well the H I systems with  $N_{\text{HI}} \lesssim 10^{16} \text{ cm}^{-2}$  (see Figure 9), so the flattening should likely occur between  $10^{16}$  and  $10^{17} \text{ cm}^{-2}$ . The  $\log N_{\text{HI}} = [17.7, 18]$  interval will likely remain largely unconstrained owing to the difficulty in measuring  $N_{\text{HI}}$  in this regime requiring either to fit the Lyman series lines (e.g., Lehner et al. 2009a) or to have very high quality S/N data to discern the damping wings in the Lyman- $\alpha$  absorption.

In Figure 9 we also show one of the  $f(N_{\text{HI}})$  models in the local universe by Corbelli & Bandiera (2002) (long-dashed orange curve; see their Figure 2 where we adjusted vertically their model to fit the DLA and SLLS distributions – the model with  $f(N_{\text{H}}) \propto N_{\text{H}}^{-3.3}$  is shown). In their models, they investigated if the flattening of  $f(N_{\text{HI}})$  between the LLSs and DLAs could be explained if  $f(N_{\text{H}})$  ( $\text{H} = \text{H I} + \text{H II}$ ) follows a single power law, while  $f(N_{\text{HI}})$  can deviate from a single power owing to the change of the ionization fraction as function of  $N_{\text{HI}}$ . While the low  $N_{\text{HI}}$  systems are not well matched (in part because they attempted to fit data based on equivalent width measurements), the higher column density regimes are quite remarkably well reproduced. Other models explored the self-shielding effect on the  $f(N_{\text{HI}})$  of DLAs and LLSs using spherical isothermal gaseous halos (Murakami & Ikeuchi 1990; Petitjean et al. 1992; Zheng & Miralda-Escudé 2002), which yields a somewhat similar functional form. Hence photoionization of a single power law population in  $f(N_{\text{HI}})$  could be the main cause for the complicated shape of the  $f(N_{\text{HI}})$  distribution.

In the higher redshift regime, Petitjean et al. (1993) also noted that a single  $f(N_{\text{HI}})$  over the entire  $N_{\text{HI}}$  regime was not statistically adequate, and, in particular, their data hinted as well to two flattenings in the column density distribution function, one in the PLLS regime and the other one in LLS/SLLS regime that they explained as transitions between the H I systems to metal absorbers and between the neutral and ionized systems, respectively. The most recent study on  $f(N_{\text{HI}})$  at  $z \sim 3.7$ , by Prochaska et al. (2010) suggests an even more complicated  $f(N_{\text{HI}})$  distribution. We show in Figure 9 their  $f(N_{\text{HI}})$  distribution over the same range of H I column density. We emphasize that while the Lyman- $\alpha$  forest (up to  $\log N_{\text{HI}} \lesssim 14$ ), SLLS, DLA, and to a lesser extent LLS distributions are relatively well constrained, the PLLSs and H I interval  $14 \lesssim \log N_{\text{HI}} \lesssim 16$  are not (see their Figure 14 for the amplitude of possible  $f(N_{\text{HI}})$  in each  $N_{\text{HI}}$  region). As already mentioned above, there appears to be no evolution in the DLA portion of  $f(N_{\text{HI}})$  with redshift, and a steeper slope than found by Rao et al. (2006) seems more appropriate for connecting the DLAs and SLLSs at low- $z$ . While a similar flattening is observed in the SLLS regime, in the low- $z$  universe  $f(N_{\text{HI}})$  appears (tentatively) even flatter. A larger sample of SLLSs will be needed to confirm this as other explanations (e.g., an evolving normalization at different mean redshift or the presence of another inflection point) could account for the observed behavior.

In the lower  $N_{\text{HI}}$  regime,  $f(N_{\text{HI}})$  appears to evolve from the high to low- $z$  universe. At  $\log N_{\text{HI}} \leq 14.5$ , where  $f(N_{\text{HI}})$  is well constrained at both low and high  $z$ , the slope becomes steeper as  $z$  decreases and there is a drop in the number of systems with redshift. Without a steep decline in the UV background flux (stemming from a drop of the number of QSOs at low  $z$ ), the number of systems would be predicted to be much lower at low  $z$ , suggesting that the changes in the UV background may be the dominant reason for the evolution of the Lyman- $\alpha$  forest (e.g., Theuns et al. 2002b). Numerical simulations of a cold dark matter universe with a photoionized background dominated by the QSO light can, indeed, reproduce these properties to some extents (e.g., Theuns et al. 2002b; Davé et al. 2010), but the observed evolution rate of  $\beta$  is smaller than predicted. Part of the discrepancy between the models and observations could be due to the models ignoring the galactic contribution to the UV background, or more generally to an uncertainty in the strength and shape of the UV background. Large-scale galactic outflows could be thought as another uncertainty because (in the regime where  $\log N_{\text{HI}} > 14$ ) they likely increase the H I absorbing cross section via deposit of cool gas in the outermost edges of galactic halos (Davé et al. 2010). Cosmological simulations however, suggest that galactic feedback has little impact on  $f(N_{\text{HI}})$  of the Lyman- $\alpha$  forest as they only fill a small fraction of the volume, leaving the IGM filaments unscathed (Theuns et al. 2002a). Hence, the possible differences seen at  $14.5 \lesssim \log N_{\text{HI}} \lesssim 19$  may occur owing to the evolution of both the UV background and galactic feedback. Current and future efforts to provide better statistics for the PLLSs and LLSs at both low and high- $z$  should provide direct constraints on the UV background evolution and cosmological simulations.

## 6. LLSS AND THE GASEOUS HALOS OF GALAXIES

At very low redshift, the connection between LLSs, galaxies, and large-scale structures has been examined for a small number of individual systems discovered using *HST* and the *Far Ultraviolet Spectroscopic Explorer (FUSE)*. These studies have found LLSs associated with individual galaxies ( $0.2L_* \lesssim L \lesssim 3.4L_*$ ) at impact parameters  $\rho \sim 30 - 100 \text{ kpc}$  (Chen & Prochaska 2000; Jenkins et al. 2003; Tripp et al. 2005; Cooksey et al. 2008; Lehner et al. 2009a). Some low redshift LLSs are metal enriched (i.e.,  $Z \gtrsim 0.3Z_{\odot}$ , e.g., Chen & Prochaska 2000; Prochaska et al. 2006b; Lehner et al. 2009a) while some are relatively metal-poor (i.e.,  $Z \lesssim 0.1Z_{\odot}$ , e.g., Prochaska & Burles 1999; Cooksey et al. 2008; Zonak et al. 2004). The presence of metal-enriched material far from the central star forming regions of galaxies suggests some LLSs are sensitive to the nature of feedback in galaxies. The existence of extremely metal-poor systems suggests the gas probed by some LLS absorption originates outside of galaxies, perhaps tracing IGM matter falling onto a galaxy. An example of a LLS tracing very low metallicity ( $Z \sim 0.02Z_{\odot}$ ) gas falling onto a near solar,  $0.3L_*$  galaxy at  $z \sim 0.274$  will be described in J. Ribaudo et al. (in prep.). In addition to the observational evidence, numerical simulations also predict a physical association of LLSs with the gravitational potential of galaxies. These simulations show LLSs arising from infalling streams of intergalactic gas as well as out-

flowing gas ejected from galaxies due to stellar feedback (Gardner et al. 2001; Dekel & Birnboim 2006; Kohler & Gnedin 2007; Keres et al. 2009; Kacprzak et al. 2010, Fumagalli et al. 2011, Stewart et al. 2011; but also see, Mo & Miralda-Escudé 1996; Maller et al. 2003).

Based on these observational and theoretical studies, LLSs appear to be associated with circumgalactic environments. With this knowledge, we can calculate the characteristic sizes of such gaseous galactic envelopes using our survey of LLSs and knowledge of the galaxy population with which they are associated. We rewrite  $l(X) \propto n_{\text{LLS}}\sigma_{\text{LLS}}$  as:

$$l(X)_{\text{LLS}} \propto n_{\text{GAL}}\sigma_{\text{GAL}}, \quad (14)$$

where  $n_{\text{GAL}}$  is the comoving number density of galaxies giving rise to LLS absorption and  $\sigma_{\text{GAL}}$  is the projected physical cross section of galaxies to columns  $\log N_{\text{HI}} \geq 17.5$  (for comparison with R2,RP10 samples). The comoving number density of galaxies at a given redshift is calculated from the integration of an observationally constrained galaxy luminosity function. We investigate the size of absorbers assuming only galaxies with  $L \geq L_{\text{min}}$  give rise to LLS absorption. Thus, following Tytler (1987), we rewrite Equation 14 as:

$$l(X) = \frac{c}{H_0} \int_{L_{\text{min}}}^{\infty} f_c \pi R^2(L) \Phi(L) dL, \quad (15)$$

where  $f_c \pi R^2(L)$  is the cross section for absorption,  $\sigma_{\text{GAL}}$ , with a covering factor  $f_c$  and  $\Phi(L) dL = \Phi_*(L/L_*)^\alpha \exp(-L/L_*) d(L/L_*)$  is the assumed form of the galaxy luminosity function (Schechter 1976). The comoving number density of galaxies that contribute to the LLS population is determined by our choice of  $L_{\text{min}}$ , and we use all galaxies with  $L \geq L_{\text{min}}$  in this estimation of the mean  $\sigma_{\text{GAL}}$ . We note that several previous treatments of the gaseous halos around galaxies have allowed for a Holmberg-like scaling of the physical extent of the gas with  $R(L) = R_*(L/L_*)^{\beta_L}$ , where  $R_*$  is the projected radial extent of the absorbing gas associated with an  $L_*$  galaxy (Tytler 1987). Numerous galaxy-absorber studies have shown if the radial extent of galaxies is allowed to scale with luminosity,  $R(L)$  serves as the effective cutoff for observed absorption out to that projected distance (i.e., Kacprzak et al. 2010; Chen et al. 2010; Kacprzak et al. 2008; Chen et al. 2001). However, we are considering the physical extent of absorbing gas averaged over all galaxy types and sizes, with our only selection criterion being  $L \geq L_{\text{min}}$ , and over a very wide range in redshift. Over time, the galaxies giving rise to LLSs may be best described with an evolving  $\beta_L$ , but as we are generalizing our analysis to the size of the gaseous envelope around a “mean” galaxy, averaged over all morphologies, star formation properties, sizes, etc., we adopt  $\beta_L = 0.0$ . Our results therefore describe the mean extent of circumgalactic gas about galaxies  $L \geq L_{\text{min}}$ .

Equation 15 can be solved using the incomplete  $\Gamma$  function, giving the statistical absorption radius of a galaxy

$$R_s = f_c^{0.5} R = \left[ \frac{c\pi\Phi_*}{H_0 l(X)} \Gamma \left( 2\beta_L + \alpha + 1, \frac{L_{\text{min}}}{L_*} \right) \right]^{-0.5}. \quad (16)$$

The radius  $R_s$  is therefore the mean radial extent of gas about an average host galaxy scaled by  $f_c^{0.5}$ , while

$\pi R_s^2 = \sigma_{\text{GAL}}$  is the projected area of such a galaxy for which  $\log N_{\text{HI}} \geq 17.5$  for a given choice of  $L_{\text{min}}$ . We plot  $R_s$  in Figure 10 as a function of the assumed  $L_{\text{min}}$  in the left panel and redshift in the right panel. In the left panel, the shaded regions correspond to different luminosity function parameters, which are appropriate for the redshift ranges given in the legend. The luminosity function parameters are observationally determined and restricted to the redshift range probed by each survey. The right panel shows the statistical absorption radius as a function of redshift for three snapshots of  $L_{\text{min}}$ . The width of the shaded regions is determined from the redshift range of the survey used to calculate the luminosity function. The height of each region spans the  $R_s$  value predicted for the range in redshift. The recent study of Mg II absorbers and galaxies at  $z < 0.5$  by Chen et al. (2010) found  $f_c = 0.70$  for the strongest Mg II absorbers out to  $R_* = 75$  kpc (with  $\beta_L = 0.35$ ). The introduction of a non-unity covering factor will thus increase the values for  $R$  by  $\sim 10\text{--}30\%$  compared with  $R_s$ .

From Figure 10, we can draw several inferences about the evolution and properties of the galactic environments giving rise to LLS absorption, albeit with some limitations. We are describing the mean extent of  $\tau \geq 2$  H I gas with no assumptions about which galaxies give rise to the absorption. The evolution in  $R_s$  does not track the evolution of individual galaxies, only the mean galaxy with  $L \geq L_{\text{min}}$  for each  $z$ . Any change in the physical cross section for the mean galaxy at each redshift does not imply individual galaxies are evolving on that timescale, as it is likely the case the galaxies giving rise to LLSs at  $z \sim 5$  are not the same galaxies giving rise to LLSs at  $z \sim 1$ . With these limitations in mind, several inferences can be drawn from this approach.

The  $L \geq L_*$  galaxies alone cannot account for the observed population of LLSs, because  $R_s$  would be inconsistent with previous galaxy-absorber observations, especially at  $z \geq 2$  where the sizes implied for LLSs would be quite large compared with observations (Steidel et al. 2010). Extending the integration of Equation 15 to sub- $L_*$  galaxies produces  $R_s$  values more consistent with the impact parameters found independently by other studies (e.g. Bouché et al. 2007; Kacprzak et al. 2010; Chen et al. 2010). It is not clear how small  $L_{\text{min}}$  should be before we can account for the entire population of LLSs, but Figure 10 highlights the importance and need for deep observations of QSO fields to confidently relate absorbers to specific galaxies. This conclusion is not surprising as Mg II studies and individual LLS observations show sub- $L_*$  ( $0.25 \lesssim L/L_* \lesssim 0.76$ ) galaxies contribute to the population of optically thick absorbers (e.g. Steidel et al. 2010; Kacprzak et al. 2010; Chen et al. 2010; Lehner et al. 2009a; Kacprzak et al. 2008). However, our analysis suggests the less luminous galaxy population may be the dominant source of LLSs. A similar scenario has been suggested for Mg II absorbers over the redshifts  $0.37 \leq z \leq 0.82$ , where Caler et al. (2010) find evidence that at least 70–75% of the Mg II absorber host galaxies are fainter than  $0.56L_*$ .

Figure 10 also highlights a significant evolution in the physical cross section of the mean absorbing galaxy as a function of redshift. For  $L_{\text{min}} \sim 0.1L_*$ ,  $R_s$  decreases by a factor of  $\sim 3$  from  $z \sim 5$  to 2, but remains relatively constant from  $z \sim 2$  to 0.3. This is remarkable as it suggests

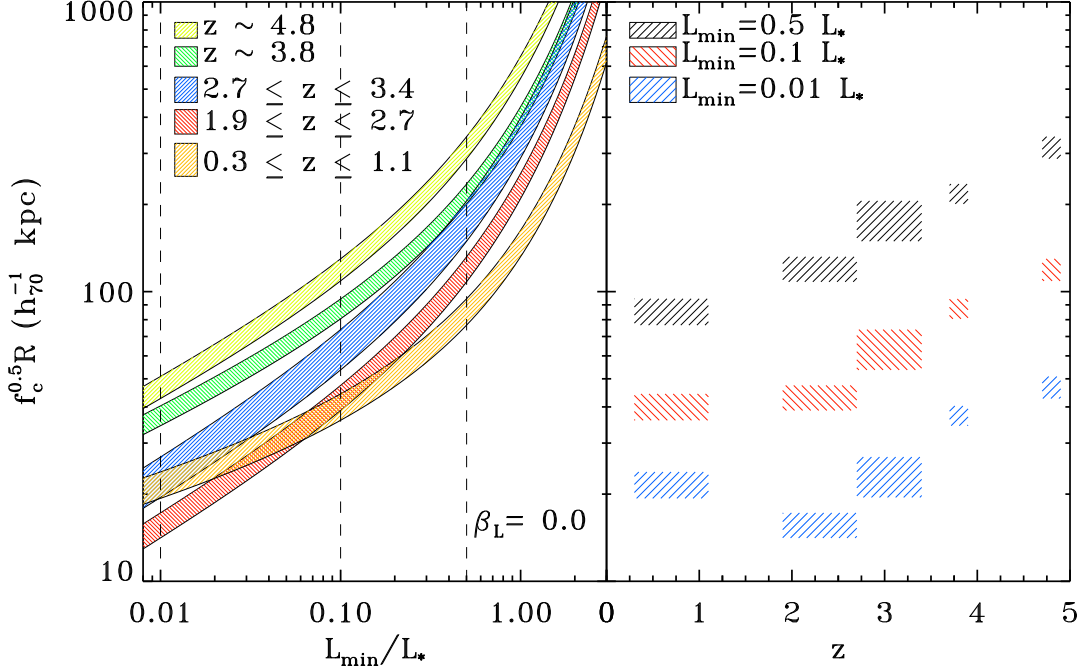


FIG. 10.— The left panel shows the statistical absorption distance ( $f_c^{0.5} R$ ) plotted against  $L_{\min}/L_*$ , where  $L_{\min}$  is the assumed minimum luminosity for a galaxy to give rise to LLS absorption (see Equation 16). The shaded areas represent the absorption distance for specific redshift ranges, each with different luminosity function parameters. The orange region corresponds to the average  $\alpha$  and  $\Phi_*$  values determined by Faber et al. (2007) using DEEP2 over the redshift range  $0.3 \lesssim z \lesssim 1.1$ . The red and blue regions correspond to the analysis of Reddy & Steidel (2009) over the redshift range  $1.9 \lesssim z \lesssim 2.7$  and  $2.7 \lesssim z \lesssim 3.4$ , respectively. Lastly, the green and yellow regions correspond to the analysis of van der Burg et al. (2010) using the CFHT Legacy Survey Deep fields at redshifts  $z \sim 3.8$  and  $z \sim 4.8$ . The right panel shows the evolution of the statistical absorption distance as a function of redshift. The colored shaded regions correspond to a minimum luminosity cut designated in the left panel with the dashed lines. The width of the regions corresponds to the redshift range probed by the particular survey used to calculate the galaxy luminosity function and the height of the regions correspond to the range in  $R_s$  seen as we vary the redshift over the acceptable range. Note the evolution in the physical size of absorbers in the right panel does not imply single galaxies are evolving on the same timescale. Rather, the right panel implies the physical size of the gaseous envelope of a mean galaxy at a specific redshift undergoes significant evolution over cosmic time.

the physical cross section of the gaseous envelopes of a mean galaxy has decreased significantly over a very short epoch, but for the majority of cosmic time the physical extent of gas about a mean galaxy has been fairly constant. This relatively constant nature of absorption cross section at low- $z$  was also noted by Nestor et al. (2005), who found evidence for little evolution in the physical size of Mg II absorbers as a function of redshift over  $0.3 \leq z \leq 1.2$  (for  $0.001 \leq L_{\min}/L_* \leq 0.25$ ).

Changes in physical cross section can be brought on by evolution in the typical covering factor as well as typical radial extent. However, changes in  $f_c$  alone likely cannot be responsible for the large drop in the physical cross section of the mean galaxy given the typical values observed at low redshift. While a change in the typical radial extent,  $R$ , is a likely cause, other factors could influence our perception of the cross section for the mean galaxy at a given redshift. Evolution in the power law index,  $\beta_L$ , associated with changes in the relative fraction of high versus low luminosity galaxies giving rise to LLSs could alter the mean cross section calculated here. For example, if at high redshifts ( $z \sim 5$ ) the majority of LLSs arise in the circumgalactic gas of relatively high mass, bright galaxies, but at low redshifts ( $z \sim 0.3 - 1$ ) the majority of LLSs arise in the environments of low mass, relatively low luminosity galaxies, we would expect an evolution in the mean physical cross section of LLS absorption simi-

lar to what is shown in Figure 10. An evolution in  $L_{\min}$  with redshift would have an affect similar to an evolving  $\beta_L$ .

As we alluded to above, there are two commonly invoked scenarios for producing circumgalactic gas at such large distances from the central regions of galaxies. In the first, galactic-scale outflows drive gas to large radial distances from the main body of a galaxy providing for Mg II and LLS absorption (Bouché et al. 2006). Evidence for this has been presented by Bouché et al. (2007), who found starburst galaxies within 50 kpc for  $\sim 70\%$  of a sample of strong Mg II absorbers. Prochter et al. (2006) have also argued the importance of outflows to Mg II selected systems based on the similarity in the evolution in the redshift incidence of strong Mg II absorbers and the star formation rate density of the Universe for  $z < 2$ . Combined with constraints on the size of the galaxies giving rise to the Mg II absorption, this suggests such systems are produced through feedback processes in low mass galactic halos. In addition, other recent works have connected Mg II selected absorbers to galactic outflows at  $z \sim 0.7$  (Nestor et al. 2010),  $0.5 < z < 1.4$  (Ménard & Chelouche 2009), and  $2 \lesssim z \lesssim 3$  (Steidel et al. 2010).

The second scenario assumes much of the circumgalactic material traced by LLSs is intergalactic gas being accreted onto the galaxies. To maintain the low

apparent ionization conditions of LLSs (Lehner et al. 2009a; Cooksey et al. 2008), the gas should not be shock heated as it is accreted. Such low-ionization gas falls under the phenomenon of cold mode accretion (CMA) (Kereš et al. 2005) predicted to be directed along the filamentary structure of the Universe, allowing galaxies to draw gas from large distances. CMA can account for the observational properties of galaxies inconsistent with the traditional shock-heated accretion models, such as the color bimodality of galaxies and the decline of the cosmic star formation rate at low redshifts (Kereš et al. 2005; Dekel & Birnboim 2006; Dekel et al. 2009a,b; Kereš et al. 2009). Support for CMA has been suggested in recent studies of Mg II absorbers where no correlation between the Mg II absorption strength and galaxy color was found, indicating the origin of the absorbers is not tied to the star formation history of the associated galaxy (Chen et al. 2010). Chen et al. (2010) conclude Mg II absorbers (and LLSs as an extension) are a generic feature of galaxy environments and that the gas probed by Mg II absorption is likely intergalactic in origin. There is more direct observational evidence to support this origin for some LLSs. The nearly primordial LLS detected by J. Ribaudo et al. (in prep.) within 40 kpc of a near solar galaxy is similar in ionization state and metallicity to the low-metallicity absorbers reported in Cooksey et al. (2008) and Zonak et al. (2004).

While outflows and infall must play an important role in the composition and maintenance of circumgalactic environments, observations of a few systems suggest gas ejected to large distances during galaxy mergers and tidal interactions could also be responsible for some of the observed LLSs (e.g., Jenkins et al. 2003; Lehner et al. 2009a). Other studies have suggested the high velocity clouds (HVCs) seen about the Milky Way may be analogs for the higher redshift LLSs or Mg II systems (Charlton et al. 2000; Richter et al. 2009; Stocke et al. 2010). In the Milky Way and the nearby Magellanic Clouds, the HVCs probe outflows related to galactic fountains and winds (Keeney et al. 2006; Zech et al. 2008; Lehner & Howk 2007; Lehner et al. 2009b), the infall of low-metallicity gas (e.g., Wakker 2001; Wakker et al. 2008; Thom et al. 2008), and the tidal debris stripped from the Magellanic Clouds (and others) as they interact with each other and the Milky Way (e.g., Putman et al. 2003). Thus, these potential LLS analogs have a wide range of origins, although many of the Milky Way HVCs tend to reside at much smaller impact parameters than suggested for the LLSs ( $\rho \leq 10 - 20$  kpc Lehner & Howk 2010; Wakker et al. 2008; Thom et al. 2008). On the other hand tidal remnants from galactic interactions or gas outflows from its satellites are about 50–100 kpc from the Milky Way. These local analogs underline the complex task in defining what kind of phenomena the LLSs trace and if one dominates over the others.

Discriminating between these scenarios using only the correlations of redshifts and equivalent widths of the Mg II lines with other parameters has been difficult. The availability of H I column density information for a large number of LLSs offers a path to studying the metallicities of the LLSs/Mg II systems at low redshifts. Further studies specifically targeting the galactic environments of LLSs, where the metallicities of the LLSs and the galaxies

can be compared, will be critical to further characterize the nature of the absorbers and the role these systems play in the movement of gas into and out of the halos of galaxies. With metallicity playing a fundamental role in discriminating between these two scenarios (e.g., Fumagalli et al. 2011), absorbers will need to be selected based on H I absorption to provide a comprehensive picture of the nature and origin of circumgalactic gas.

## 7. SUMMARY AND CONCLUDING REMARKS

Using FOS and STIS *HST* archival observations, we have compiled the largest sample of QSOs to date with coverage of the Lyman limit over the redshift range  $0.24 \leq z \leq 2.59$ . We have used these observations to study the population of LLSs over these redshifts. In considering candidates for our R1 (R2) sample, we included only the data from objects where the spectral quality was judged to be sufficient to reliably detect a LLS with  $\tau_{\text{LLS}} \geq 1$  ( $\tau_{\text{LLS}} \geq 2$ ). The sample R1 (R2) contains 229 (249) QSOs, covering a total redshift path of  $\Delta z = 79$  (96) and a total of 61 (50) LLSs. This marks a factor of  $\sim 3 - 4$  increase in the number of LLSs and redshift path sampled over the most up-to-date work by Stengler-Larrea et al. (1995) and Jannuzzi et al. (1998) in this redshift regime. In addition to our statistical sample, we have catalogued 206 low redshift LLSs from the FOS and STIS archives, which increases the sample of LLSs by a factor of  $\sim 10$  for the  $z \leq 2.6$  sample. The robustness of our samples allowed us to examine the evolution of LLSs over  $0.24 \leq z \leq 2.59$  for the R1 and R2 samples and from  $0.2 \lesssim z \lesssim 5.0$  for the RP10 sample that combines our R2 sample with the high redshift sample of Prochaska et al. (2010). Our main results are as follows:

1. We find the redshift density to be well fitted by the power law  $l(z) \propto (1+z)^\gamma$  (Equation 7). We find for sample R1 (R2)  $\gamma = 1.19 \pm 0.56$  ( $1.33 \pm 0.61$ ). For the RP10 sample at  $z \leq 5$ ,  $l(z)$  is well modeled by a single power law with  $\gamma = 1.83 \pm 0.21$  (for  $\tau_{\text{LLS}} \geq 2$ ).
2. Assuming a standard  $\Lambda\text{CDM}$  cosmology with our RP10 sample, we find  $l(X)$ , which is proportional to the product of the comoving number density of absorbers,  $n_{\text{LLS}}$ , and the average physical size of an absorber,  $\sigma_{\text{LLS}}$ , decreases by a factor 1.5 from  $z \sim 5$  to 3. The evolution of  $l(X)$  at  $z \leq 2.6$  has slowed considerably, decreasing by a similar factor for  $z \sim 2.6$  to 0.25. This indicates the environments which give rise to LLSs experienced dramatic changes in the first  $\sim 2$  Gyr after  $z \sim 5$ , then more slowly evolved over the following  $\sim 8$  Gyr.
3. We calculate the average proper distance,  $\Delta r_{\text{LLS}}$ , a photon travels before encountering a  $\tau_{\text{LLS}} \geq 2$  LLS and compare this result with the predicted mean free path of hydrogen ionizing photons. The ratio of  $\Delta r_{\text{LLS}}$  and the mean free path from  $z \sim 5$  to 0 suggests the  $\tau_{\text{LLS}} < 2$  absorption systems have become increasingly more important for absorption of Lyman continuum photons as the Universe has evolved.
4. We model the column density distribution function,  $f(N_{\text{HI}})$ , for the various  $N_{\text{HI}}$  regimes at  $z \leq 2.6$

using a functional form  $f(N_{\text{HI}}) \propto N_{\text{HI}}^{-\beta}$ . We show that a single power law cannot fit the entire observed  $N_{\text{HI}}$  regime. Instead several slopes are needed. For the LLSs, we derive  $\beta \sim 1.9$ . The functional form in the Lyman- $\alpha$  forest regime ( $\beta = 1.72 \pm 0.02$ ) and in the SLLS regime ( $\beta \sim 0.8$ ) suggests the distribution has two inflection points. For the DLA regime,  $\beta \sim 1.8$  seems appropriate for connecting  $f(N_{\text{HI}})$  between the DLAs and SLLSs. Simple models assuming a single power law in  $f(N_{\text{H}})$  with absorbers photoionized by the UV background reproduce the  $f(N_{\text{HI}})$  distribution remarkably well.

5. We observe little redshift evolution in  $f(N_{\text{HI}})$  for the SLLSs and DLAs from high ( $z \sim 3.7$ ) to low ( $z \leq 2.6$ ) redshifts. However, there is evidence that  $f(N_{\text{HI}})$  evolves from high to low redshift at  $\log N_{\text{HI}} \lesssim 17.7$ , which coincides with the strong evolution seen in the UV background and star-formation rates of galaxies over similar redshifts.

## REFERENCES

Bahcall, J. N., & Peebles, P. J. E. 1969, ApJ, 156, L7

Bechtold, J., Dobrzycki, A., Wilden, B., Morita, M., Scott, J., Dobrzycka, D., Tran, K.-V., & Aldcroft, T. L. 2002, ApJS, 140, 143

Bouché, N., Murphy, M. T., Péroux, C., Davies, R., Eisenhauer, F., Förster Schreiber, N. M., & Tacconi, L. 2007, ApJ, 669, L5

Bouché, N., Murphy, M. T., Péroux, C., Csabai, I., & Wild, V. 2006, MNRAS, 371, 495

Caler, M. A., Sheth, R. K., & Jain, B. 2010, MNRAS, 406, 1269

Charlton, J. C., & Churchill, C. W. 1998, ApJ, 499, 181

Charlton, J. C., Churchill, C. W., & Rigby, J. R. 2000, ApJ, 544, 702

Chen, H.-W., Helsby, J. E., Gauthier, J.-R., Shectman, S. A., Thompson, I. B., & Tinker, J. L. 2010, ApJ, 714, 1521

Chen, H.-W., Lanzetta, K. M., & Webb, J. K. 2001, ApJ, 556, 158

Chen, H.-W., & Prochaska, J. X. 2000, ApJ, 543, L9

Churchill, C. W., Mellon, R. R., Charlton, J. C., Jannuzzi, B. T., Kirhakos, S., Steidel, C. C., & Schneider, D. P. 2000, ApJS, 130, 91

Churchill, C., Steidel, C., & Kacprzak, G. 2005, Extra-Planar Gas, 331, 387

Cooksey, K. L., Prochaska, J. X., Chen, H.-W., Mulchaey, J. S., & Weiner, B. J. 2008, ApJ, 676, 262

Corbelli, E., & Bandiera, R. 2002, ApJ, 567, 712

Danforth, C. W., & Shull, J. M. 2008, ApJ, 679, 194

Davé, R., Oppenheimer, B. D., Katz, N., Kollmeier, J. A., & Weinberg, D. H. 2010, MNRAS, 408, 2051

Dekel, A., Sari, R., & Ceverino, D. 2009a, ApJ, 703, 785

Dekel, A., et al. 2009b, Nature, 457, 451

Dekel, A., & Birnboim, Y. 2006, MNRAS, 368, 2

Faber, S. M., et al. 2007, ApJ, 665, 265

Faucher-Giguère, C.-A., Lidz, A., Zaldarriaga, M., & Hernquist, L. 2009, ApJ, 703, 1416

Fumagalli, M., Prochaska, J. X., Kasen, D., Dekel, A., Ceverino, D., & Primack, J. R. 2011, arXiv:1103.2130

Gardner, J. P., Katz, N., Hernquist, L., & Weinberg, D. H. 2001, ApJ, 559, 131

Haardt, F., & Madau, P. 1996, ApJ, 461, 20

Janknecht, E., Reimers, D., Lopez, S., & Tytler, D. 2006, A&A, 458, 427

Jannuzzi, B. T., et al. 1998, ApJS, 118, 1

Jena, T., et al. 2005, MNRAS, 361, 70

Jenkins, E. B., Bowen, D. V., Tripp, T. M., Sembach, K. R., Leighly, K. M., Halpern, J. P., & Lauroesch, J. T. 2003, AJ, 125, 2824

Kacprzak, G. G., Churchill, C. W., Ceverino, D., Steidel, C. C., Klypin, A., & Murphy, M. T. 2010, ApJ, 711, 533

Kacprzak, G. G., Churchill, C. W., Steidel, C. C., & Murphy, M. T. 2008, AJ, 135, 922

Keeney, B. A., Danforth, C. W., Stocke, J. T., Penton, S. V., Shull, J. M., & Sembach, K. R. 2006, ApJ, 646, 951

Kereš, D., & Hernquist, L. 2009, ApJ, 700, L1

Kereš, D., Katz, N., Weinberg, D. H., & Davé, R. 2005, MNRAS, 363, 2

Kereš, D., Katz, N., Fardal, M., Davé, R., & Weinberg, D. H. 2009, MNRAS, 395, 160

Keyes, C. D., Koratkar, A. P., Dahlem, M., Hayes, J., Christensen, J., & Martin, S. 1995, v6.0

Kohler, K., & Gnedin, N. Y. 2007, ApJ, 655, 685

Komatsu, E., et al. 2009, ApJS, 180, 330

Kulkarni, V. P., Khare, P., Péroux, C., York, D. G., Lauroesch, J. T., & Meiring, J. D. 2007, ApJ, 661, 88

Lanzetta, K. M. 1991, ApJ, 375, 1

Lehner, N., & Howk, J. C. 2010, ApJ, 709, L138

Lehner, N., Prochaska, J. X., Kobulnicky, H. A., Cooksey, K. L., Howk, J. C., Williger, G. M., & Cales, S. L. 2009a, ApJ, 694, 734

Lehner, N., Staveley-Smith, L., & Howk, J. C. 2009b, ApJ, 702, 940

Lehner, N., Savage, B. D., Richter, P., Sembach, K. R., Tripp, T. M., & Wakker, B. P. 2007, ApJ, 658, 680

Lehner, N., & Howk, J. C. 2007, MNRAS, 377, 687

Lehner, N., Savage, B. D., Wakker, B. P., Sembach, K. R., & Tripp, T. M. 2006, ApJS, 164, 1

Maller, A. H., Prochaska, J. X., Somerville, R. S., & Primack, J. R. 2003, MNRAS, 343, 268

Ménard, B., & Chelouche, D. 2009, MNRAS, 393, 808

Miralda-Escudé, J., Cen, R., Ostriker, J. P., & Rauch, M. 1996, ApJ, 471, 582

Mo, H. J., & Miralda-Escudé, J. 1996, ApJ, 469, 589

Murakami, I., & Ikeuchi, S. 1990, PASJ, 42, L11

Nagamine, K., Choi, J.-H., & Yajima, H. 2010, arXiv:1006.5345

Nestor, D. B., Johnson, B. D., Wild, V., Ménard, B., Turnshek, D. A., Rao, S., & Pettini, M. 2010, arXiv:1003.0693

Nestor, D. B., Turnshek, D. A., & Rao, S. M. 2005, ApJ, 628, 637

O'Meara, J. M., in prep.

O'Meara, J. M., Prochaska, J. X., Burles, S., Prochter, G., Bernstein, R. A., & Burgess, K. M. 2007, ApJ, 656, 666

Penton, S. V., Stocke, J. T., & Shull, J. M. 2004, ApJS, 152, 29

Péroux, C., Dessauges-Zavadsky, M., D'Odorico, S., Sun Kim, T., & McMahon, R. G. 2005, MNRAS, 363, 479

Péroux, C., Dessauges-Zavadsky, M., D'Odorico, S., Kim, T.-S., & McMahon, R. G. 2003, MNRAS, 345, 480

6. Assuming LLSs arise in circumgalactic gas, we find the physical cross section of the mean galaxy at each redshift to LLS absorption decreased by a factor of  $\sim 9$  from  $z \sim 5$  to 2 and subsequently stayed relatively constant. We argue sub- $L_*$  galaxies must contribute significantly to the absorber population.

The authors wish to thank J.X. Prochaska who kindly made their data available for comparison with this sample prior to publication. We would also like to thank the referee for useful and insightful comments, as well as J.X. Prochaska and J. O'Meara for their valuable comments. Support for this research was provided by NASA through grant HST-AR-11762.01-A from the Space Telescope Science Institute, which is operated by the Association of Universities for Research in Astronomy, Incorporated, under NASA contract NAS5-26555. Further support comes from NASA grant NNX08AJ31G. This research has made use of the NASA Astrophysics Data System Abstract Service and the Centre de Données de Strasbourg (CDS).

Péroux, C., Dessauges-Zavadsky, M., Kim, T., McMahon, R. G., & D'Odorico, S. 2002, *Ap&SS*, 281, 543

Petitjean, P., Webb, J. K., Rauch, M., Carswell, R. F., & Lanzetta, K. 1993, *MNRAS*, 262, 499

Petitjean, P., Bergeron, J., & Puget, J. L. 1992, *A&A*, 265, 375

Petitjean, P., & Bergeron, J. 1990, *A&A*, 231, 309

Prochaska, J. X., O'Meara, J. M., & Worseck, G. 2010, *ApJ*, 718, 392

Prochaska, J. X., Worseck, G., & O'Meara, J. M. 2009, *ApJ*, 705, L113

Prochaska, J. X., Weiner, B. J., Chen, H.-W., & Mulchaey, J. S. 2006a, *ApJ*, 643, 680

Prochaska, J. X., O'Meara, J. M., Herbert-Fort, S., Burles, S., Prochter, G. E., & Bernstein, R. A. 2006b, *ApJ*, 648, L97

Prochaska, J. X., & Wolfe, A. M. 2009, *ApJ*, 696, 1543

Prochaska, J. X., Chen, H.-W., Howk, J. C., Weiner, B. J., & Mulchaey, J. 2004, *ApJ*, 617, 718

Prochaska, J. X., & Burles, S. M. 1999, *AJ*, 117, 1957

Prochter, G. E., Prochaska, J. X., & Burles, S. M. 2006, *ApJ*, 639, 766

Putman, M. E., Staveley-Smith, L., Freeman, K. C., Gibson, B. K., & Barnes, D. G. 2003, *ApJ*, 586, 170

Rao, S. M., Turnshek, D. A., & Nestor, D. B. 2006, *ApJ*, 636, 610

Rauch, M. 1998, *ARA&A*, 36, 267

Reddy, N. A., & Steidel, C. C. 2009, *ApJ*, 692, 778

Ribaudo, J., in prep.

Richter, P., Charlton, J. C., Fangano, A. P. M., Bekhti, N. B., & Masiero, J. R. 2009, *ApJ*, 695, 1631

Sargent, W. L. W., Steidel, C. C., & Boksenberg, A. 1989, *ApJS*, 69, 703

Schechter, P. 1976, *ApJ*, 203, 297

Shull, J. M., Roberts, D., Giroux, M. L., Penton, S. V., & Fardal, M. A. 1999, *AJ*, 118, 1450

Simcoe, R. A., Sargent, W. L. W., Rauch, M., & Becker, G. 2006, *ApJ*, 637, 648

Songaila, A., & Cowie, L. L. 2010, arXiv:1007.3262

Spitzer, L. 1978, New York Wiley-Interscience

Steidel, C. C., Erb, D. K., Shapley, A. E., Pettini, M., Reddy, N., Bogosavljević, M., Rudie, G. C., & Rakic, O. 2010, *ApJ*, 717, 289

Steidel, C. C., & Sargent, W. L. W. 1992, *ApJS*, 80, 1

Stengler-Larrea, E. A., et al. 1995, *ApJ*, 444, 64

Stocke, J. T., Keeney, B. A., & Danforth, C. W. 2010, *Publications of the Astronomical Society of Australia*, 27, 256

Storrie-Lombardi, L. J., McMahon, R. G., Irwin, M. J., & Hazard, C. 1994, *ApJ*, 427, L13

Theuns, T., Viel, M., Kay, S., Schaye, J., Carswell, R. F., & Tzanavaris, P. 2002a, *ApJ*, 578, L5

Theuns, T., Zaroubi, S., Kim, T.-S., Tzanavaris, P., & Carswell, R. F. 2002b, *MNRAS*, 332, 367

Thom, C., Peek, J. E. G., Putman, M. E., Heiles, C., Peek, K. M. G., & Wilhelm, R. 2008, *ApJ*, 684, 364

Tripp, T. M., Jenkins, E. B., Bowen, D. V., Prochaska, J. X., Aracil, B., & Ganguly, R. 2005, *ApJ*, 619, 714

Tytler, D. 1982, *Nature*, 298, 427

Tytler, D. 1987, *ApJ*, 321, 49

van der Burg, R. F. J., Hildebrandt, H., & Erben, T. 2010, arXiv:1009.0758

Veron-Cetty, M. P., & Veron, P. 2010, *VizieR Online Data Catalog*, 7258, 0

Wakker, B. P., York, D. G., Wilhelm, R., Barentine, J. C., Richter, P., Beers, T. C., Ivezić, Ž., & Howk, J. C. 2008, *ApJ*, 672, 298

Wakker, B. P. 2001, *ApJS*, 136, 463

Williger, G. M., et al. 2010, *MNRAS*, 405, 1736

Wolfe, A. M., Gawiser, E., & Prochaska, J. X. 2005, *ARA&A*, 43, 861

Zech, W. F., Lehner, N., Howk, J. C., Dixon, W. V. D., & Brown, T. M. 2008, *ApJ*, 679, 460

Zheng, W., Kriss, G. A., Telfer, R. C., Grimes, J. P., & Davidsen, A. F. 1997, *ApJ*, 475, 469

Zheng, Z., & Miralda-Escudé, J. 2002, *ApJ*, 578, 33

Zonak, S. G., Charlton, J. C., Ding, J., & Churchill, C. W. 2004, *ApJ*, 606, 196

Zuo, L., & Phinney, E. S. 1993, *ApJ*, 418, 28

TABLE 1  
OBSERVATIONS FROM STIS ARCHIVE

Object	R.A. (J2000)	DEC. (J2000)	Grating	Exp. (s)	Id
J0001+0709	00 01 40.580	+07 09 54.62	G230L	2304	8569
J0012-0122	00 12 10.880	-01 22 07.74	G230L	2304	8569
J0018-3529	00 18 41.430	-35 29 04.70	G140L	2392	8287
J0021+0104	00 21 27.886	+01 04 20.10	G230L	2355	9382
J0021+0043	00 21 33.264	+00 43 00.73	G230L	2379	9382
J0021-0128A	00 21 51.800	-01 28 34.11	G230L	7900	8126
J0022-0128B	00 22 04.890	-01 28 48.07	G230L	7900	8126
J0032-2144	00 32 44.690	-21 44 22.14	G230L	5037	8225
J0038-3501	00 38 05.540	-35 01 40.35	G230L	8156	8126
J0038-3504	00 38 17.450	-35 04 05.37	G230L	11087	8126
J0039-3529	00 39 37.280	-35 29 17.10	G230L	11075	8126
J0039-3528	00 39 42.570	-35 28 00.48	G230L	8156	8126
J0043-2622	00 43 42.730	-26 22 09.17	G230L	2374	8569
J0051+0041	00 51 30.470	+00 41 49.76	G230L	2190	9051
J0100-5113	01 00 27.110	-51 13 54.21	G140L	850	9858
J0102-0853	01 02 49.610	-08 53 44.01	G230L	2150	9051
J0103-3009	01 03 55.090	-30 09 46.40	G140L	2348	8287
J0105-2736	01 05 34.770	-27 36 58.40	G230L	13266	7359
J0106+0105	01 06 03.883	+01 05 06.22	G230L	5236	9382
J0107-0019	01 07 37.049	-00 19 11.89	G230L	5252	9382
J0109-2307	01 09 02.960	-23 07 30.03	G230L	4738	8225
J0109-2102	01 09 25.130	-21 02 54.00	G140L	2289	8287
J0110+0019	01 10 56.938	+00 19 11.21	G230L	2367	9382
J0116-0043	01 16 15.528	-00 43 35.33	G230L	2363	9382
J0122+1339	01 22 31.920	+13 39 40.90	G140L	600	9067
J0123-0058	01 23 03.219	-00 58 19.38	G230L	5160	9382
J0126-2222	01 26 14.940	-22 22 33.49	G230L	4738	8225
J0126-0105	01 26 30.353	-01 05 01.03	G230L	2371	9382
J0128-3029	01 28 24.840	-30 29 41.64	G140L	1594	9506
J0132+0116	01 32 33.876	+01 16 07.10	G230L	5236	9382
J0134+0051	01 34 05.743	+00 51 09.65	G230L	5252	9382
J0137-2430	01 37 38.310	-24 30 53.70	G230L	5037	8225
J0138-0005	01 38 25.497	-00 05 33.97	G230L	5244	9382
J0139-0023	01 39 38.664	-00 23 47.80	G230L	5236	9382
J0139+0619	01 39 55.780	+06 19 22.89	G230L	8073	9894
J0139+0619	01 39 55.780	+06 19 22.89	G140L	13819	9894
J0141-0024	01 41 23.010	-00 24 21.68	G230L	2150	9051
J0145-3520	01 45 50.610	-35 20 50.05	G230L	900	9507
J0152+0023	01 52 49.687	+00 23 14.78	G230L	5260	9382
J0153+0052	01 53 09.041	+00 52 50.38	G230L	5236	9382
J0153+0009	01 53 18.101	+00 09 11.63	G230L	2379	9382
J0157-0048	01 57 33.826	-00 48 24.26	G230L	5260	9382
J0157-0106	01 57 41.563	-01 06 29.59	G140L	600	9067
J0208-0503	02 08 02.990	-05 03 00.01	G230L	2150	9051
J0210-0152	02 10 39.840	-01 52 13.53	G230L	2190	9051
J0232+3423	02 32 28.980	+34 23 46.57	G230L	2372	8569
J0240-1851	02 40 32.560	-18 51 51.26	G140L	720	9506
J0241-1514	02 41 56.500	-15 14 42.04	G230L	2304	8569
J0244-2904	02 44 49.110	-29 04 48.10	G140L	2338	8287
J0253+0107	02 53 16.464	+01 07 59.77	G230L	8141	9382
J0253-5441	02 53 29.190	-54 41 51.13	G230L	900	9507
J0256+0110	02 56 07.250	+01 10 37.92	G230L	5240	9382
J0256-3315	02 56 47.840	-33 15 26.15	G140L	2412	8569
J0304-0008	03 04 49.820	-00 08 13.60	G230L	4774	7272
J0304-0008	03 04 49.820	-00 08 13.60	G140L	23282	7575
J0308-3250	03 08 23.480	-32 50 10.19	G140L	720	9506
J0311-6039	03 11 06.880	-60 39 03.40	G140L	2520	8287
J0318-2012	03 18 25.200	-20 12 19.49	G230L	5016	8569
J0329-2357	03 29 54.070	-23 57 09.17	G230L	4798	8225
J0349-5344	03 49 28.500	-53 44 47.68	G140L	1498	9858
J0354-2724	03 54 05.570	-27 24 20.15	G230L	2376	8569
J0355-5451	03 55 13.340	-54 51 57.19	G230L	720	9507
J0411-4956	04 11 00.840	-49 56 56.38	G230L	900	9507
J0416-2056	04 16 04.340	-20 56 27.37	G230L	5053	8225
J0423-0120	04 23 15.760	-01 20 34.06	G230L	2304	8569
J0436-5258	04 36 50.790	-52 58 48.58	G140L	856	9506
J0438-2608	04 38 10.210	-26 08 38.22	G230L	720	9507
J0439-2422	04 39 09.320	-24 22 08.41	G230L	2206	8225
J0439-5311	04 39 38.661	-53 11 32.00	G140L	720	9506
J0439-4540	04 39 44.810	-45 40 42.12	G230L	7126	9894
J0439-4540	04 39 44.810	-45 40 42.12	G140L	11390	9894
J0440-5248	04 40 11.940	-52 48 18.29	G140L	720	9506
J0441-4313	04 41 17.280	-43 13 43.82	G140L	2510	9382
J0443-2820	04 43 20.760	-28 20 52.33	G230L	900	9507
J0448+0950	04 48 21.680	+09 50 52.31	G230L	4958	8569
J0452-1640	04 52 14.229	-16 40 16.76	G230L	2304	8569

TABLE 1 — *Continued*

Object	R.A. (J2000)	DEC. (J2000)	Grating	Exp. (s)	Id
J0452–2201	04 52 44.769	–22 01 20.09	G230L	2202	8225
J0453–1305	04 53 13.480	–13 05 55.84	G230L	2304	8569
J0504–2944	05 04 19.010	–29 44 39.15	G140L	720	9506
J0504–2944	05 04 19.019	–29 44 39.11	G230L	900	9507
J0509–3232	05 09 17.701	–32 32 44.97	G140L	2144	9506
J0514–3326	05 14 10.783	–33 26 22.50	G230L	16588	9165
J0732+6159	07 32 18.571	+61 59 05.43	G140L	720	9506
J0739+8146	07 39 03.389	+81 46 01.66	G230L	2726	8569
J0744+3208	07 44 17.360	+32 08 05.01	G230L	2156	9051
J0749+4152	07 49 27.907	+41 52 42.39	G140L	600	9067
J0753+4231	07 53 03.342	+42 31 30.76	G140L	600	9067
J0800+4435	08 00 06.324	+44 35 55.64	G140L	600	9067
J0800+3051	08 00 23.020	+30 51 01.26	G230L	87	9759
J0801+5210	08 01 17.750	+52 10 35.12	G140L	1543	9506
J0804+6459	08 04 30.300	+64 59 52.89	G140L	2570	7617
J0806+5041	08 06 20.460	+50 41 24.65	G230L	2420	9051
J0814+5029	08 14 35.186	+50 29 46.54	G140L	600	9067
J0825+5127	08 25 35.193	+51 27 06.40	G140L	600	9067
J0827+1052	08 27 06.509	+10 52 23.81	G230L	2304	8569
J0839+5256	08 39 52.354	+52 56 24.28	G140L	600	9067
J0857+1855	08 57 26.810	+18 55 24.20	G140L	2352	8569
J0904+1309	09 04 23.361	+13 09 21.20	G140L	2318	8287
J0912+2450	09 12 17.769	+24 50 37.70	G140L	720	9506
J0915+4426	09 15 10.748	+44 26 55.94	G140L	600	9759
J0926+3055	09 26 36.299	+30 55 06.00	G140L	576	8582
J0944+2554	09 44 42.341	+25 54 42.53	G230L	2140	8569
J0948+4323	09 48 35.922	+43 23 02.01	G230L	2333	9051
J0949+2955	09 49 41.100	+29 55 18.80	G140L	64800	8284
J0949+2955	09 49 41.100	+29 55 18.80	G230L	25920	8284
J0950+5846	09 50 11.257	+58 46 57.72	G140L	600	9067
J0950+5801	09 50 13.989	+58 01 38.00	G140L	576	8582
J0953–0038	09 53 23.588	–00 38 03.62	G230L	5248	9382
J0955+5940	09 55 11.331	+59 40 30.70	G140L	600	9067
J0958+3224	09 58 20.991	+32 24 02.37	G140L	1200	9506
J1000+0005	10 00 17.659	+00 05 22.56	G230L	2354	8569
J1001+5553	10 01 20.739	+55 53 55.10	G230L	1903	8336
J1001+5553	10 01 20.889	+55 53 49.20	G230L	1904	8336
J1001+5610	10 01 42.601	+56 10 44.00	G140L	576	8582
J1007+0042	10 07 15.472	+00 42 58.03	G230L	4731	9382
J1007+1248	10 07 26.100	+12 48 56.00	G230L	2292	9432
J1008–0223	10 08 34.739	–02 23 02.50	G140L	600	9067
J1008–0018	10 08 37.317	–00 18 35.21	G230L	5248	9382
J1009–1226	10 09 02.618	–12 26 18.14	G230L	900	9507
J1009–0026	10 09 30.421	–00 26 19.10	G230L	2383	9382
J1009+0036	10 09 45.143	+00 36 33.23	G230L	5236	9382
J1010+0003	10 10 18.160	+00 03 51.37	G230L	2375	9382
J1010–0047	10 10 33.398	–00 47 24.40	G230L	2375	9382
J1013+5615	10 13 36.299	+56 15 36.97	G140L	576	8582
J1014+4300	10 14 47.131	+43 00 30.90	G140L	2441	8287
J1017+5356	10 17 42.729	+53 56 35.39	G230L	5580	9051
J1022+3041	10 22 30.278	+30 41 04.86	G140L	2376	8569
J1022+0101	10 22 59.777	+01 01 23.20	G230L	5236	9382
J1026+6136	10 26 19.102	+61 36 28.90	G140L	600	9067
J1026+6746	10 26 32.571	+67 46 12.65	G140L	720	9506
J1028–0100	10 28 36.980	–01 00 27.86	G230L	5256	9382
J1031+5053	10 31 18.472	+50 53 36.51	G140L	2094	9506
J1031–0036	10 31 48.779	–00 36 03.28	G230L	2351	9382
J1032+5051	10 32 16.190	+50 51 20.65	G140L	1543	9506
J1032+0003	10 32 39.163	+00 03 53.39	G230L	2400	9382
J1037+0028	10 37 44.392	+00 28 08.51	G230L	2367	9382
J1040+5145	10 40 57.700	+51 45 05.86	G140L	600	9759
J1047–0047	10 47 33.395	–00 47 01.07	G230L	5248	9382
J1048+0032	10 48 52.533	+00 32 29.40	G230L	2367	9382
J1051–0051	10 51 51.460	–00 51 18.16	G140L	150	7295
J1054–0020	10 54 40.950	–00 20 49.13	G230L	2375	9382
J1057–0139	10 57 13.250	–01 39 13.90	G140L	600	9067
J1103+3715	11 03 49.709	+37 15 25.50	G230L	2188	9051
J1104–1016	11 04 16.699	–10 16 08.16	G230L	900	9507
J1106–0052	11 06 31.740	–00 52 53.52	G140L	190	7295
J1107+0048	11 07 29.022	+00 48 10.30	G230L	2383	9382
J1107+0003	11 07 36.654	+00 03 28.62	G230L	2367	9382
J1108+3133	11 08 01.300	+31 33 32.38	G230L	2200	9051
J1108–0802	11 08 12.631	–08 02 29.03	G230L	900	9507
J1109+0051	11 09 36.361	+00 51 10.40	G230L	8145	9382
J1110+4831	11 10 38.591	+48 31 16.51	G140L	720	9506
J1110+3019	11 10 40.250	+30 19 09.95	G230L	2236	9051
J1110+0048	11 10 54.906	+00 48 53.53	G230L	5244	9382

TABLE 1 — *Continued*

Object	R.A. (J2000)	DEC. (J2000)	Grating	Exp. (s)	Id
J1112+0013	11 12 56.118	+00 13 43.28	G230L	2363	9382
J1119+6004	11 19 14.352	+60 04 56.84	G140L	1000	9506
J1125+5910	11 25 53.899	+59 10 21.00	G140L	1320	9874
J1126+0034	11 26 02.783	+00 34 18.01	G230L	2371	9382
J1129-1941	11 29 30.461	-19 41 00.37	G140L	720	9506
J1137+3907	11 37 09.521	+39 07 23.59	G230L	2260	9051
J1143+3452	11 43 08.811	+34 52 22.69	G140L	10538	8287
J1200+3126	12 00 06.189	+31 26 30.20	G140L	29185	8287
J1201+0111	12 01 30.370	+01 11 38.67	G140L	1320	9874
J1203+1522	12 03 31.249	+15 22 55.50	G140L	2316	8287
J1205-2634	12 05 33.179	-26 34 03.75	G230L	4772	8225
J1209+0232	12 09 44.821	+02 32 12.70	G140L	1320	9874
J1210-2758	12 10 43.810	-27 58 59.10	G230L	5071	8225
J1214+1429	12 14 40.269	+14 29 00.10	G230L	10811	7359
J1220-2113	12 20 21.940	-21 13 15.58	G230L	4738	8225
J1220+3343	12 20 33.871	+33 43 12.53	G230L	2380	8569
J1220-0040	12 20 37.031	-00 40 33.92	G230L	5248	9382
J1224+0037	12 24 14.293	+00 37 07.90	G230L	2363	9382
J1225-2938	12 25 01.359	-29 38 19.86	G230L	5079	8225
J1225+0035	12 25 56.613	+00 35 34.01	G230L	5240	9382
J1225-0052	12 25 58.444	-00 52 27.05	G230L	5236	9382
J1226-0006	12 26 08.060	-00 06 03.10	G230L	8145	9382
J1226-2630	12 26 40.100	-26 30 01.14	G230L	4772	8225
J1228+1018	12 28 36.910	+10 18 42.16	G230L	2334	8569
J1232+5252	12 32 39.291	+52 52 50.98	G140L	600	9759
J1235+4736	12 35 31.099	+47 36 05.98	G140L	576	8582
J1238+1750	12 38 20.200	+17 50 38.90	G230L	7928	7359
J1242+0012	12 42 02.659	+00 12 28.50	G230L	7910	7359
J1246-0730	12 46 04.241	-07 30 46.74	G230L	4898	9076
J1247+3126	12 47 14.359	+31 26 41.90	G140L	4728	8287
J1249-0559	12 49 13.839	-05 59 19.26	G140L	2072	7295
J1301+5902	13 01 12.938	+59 02 06.75	G140L	120	7295
J1304-0037	13 04 24.001	-00 37 57.10	G140L	600	9067
J1313-2716	13 13 47.322	-27 16 49.09	G230L	2376	8569
J1314-3105	13 14 56.829	-31 05 55.10	G140L	2360	8287
J1317+3531	13 17 43.198	+35 31 32.00	G140L	576	8582
J1321+1106	13 21 18.878	+11 06 48.96	G230L	2304	8569
J1322+4739	13 22 39.331	+47 39 27.97	G230L	8375	8126
J1322+4739	13 22 50.720	+47 39 36.55	G230L	8327	8126
J1323-0021	13 23 23.745	-00 21 56.56	G230L	2375	9382
J1330-2056	13 30 07.657	-20 56 16.65	G140L	2394	9382
J1333+2539	13 33 09.412	+25 39 18.10	G140L	2342	8287
J1341+0059	13 41 54.236	+00 59 48.30	G230L	2359	9382
J1342+6021	13 42 13.250	+60 21 42.90	G230L	8564	7356
J1342+6021	13 42 13.250	+60 21 42.90	G140L	14778	7356
J1342-0035	13 42 46.238	-00 35 44.27	G230L	2355	9382
J1345-0023	13 45 47.820	-00 23 23.86	G230L	2350	9382
J1348+2818	13 48 11.671	+28 18 02.50	G140L	2342	8287
J1352-2649	13 52 10.302	-26 49 28.43	G230L	5079	8225
J1358-2352	13 58 32.728	-23 52 21.43	G230L	2198	8225
J1402-2822	14 02 02.289	-28 22 25.47	G230L	5071	8225
J1404-0130	14 04 45.839	-01 30 22.07	G230L	2304	8569
J1419-0036	14 19 21.017	-00 36 53.86	G230L	2375	9382
J1420-0054	14 20 50.442	-00 54 27.00	G230L	5236	9382
J1423+3252	14 23 26.122	+32 52 21.07	G230L	2376	8569
J1426+0051	14 26 50.867	+00 51 50.18	G230L	5240	9382
J1431+3952	14 31 20.541	+39 52 41.51	G230L	2292	9051
J1431-0050	14 31 43.744	-00 50 12.48	G230L	2375	9382
J1433+3131	14 33 16.051	+31 31 26.00	G140L	2364	8287
J1436-0051	14 36 45.004	-00 51 51.26	G230L	5248	9382
J1436+4952	14 36 47.629	+49 52 55.80	G230L	8375	7359
J1438-0658	14 38 16.150	-06 58 20.70	G230L	720	9507
J1438+6211	14 38 44.780	+62 11 54.39	G230L	4260	8569
J1439+2954	14 39 12.261	+29 54 49.00	G140L	2342	8287
J1445-0045	14 55 08.163	-00 45 08.39	G230L	2375	9382
J1501+0019	15 01 23.452	+00 19 39.04	G230L	2375	9382
J1502-4154	15 02 55.210	-41 54 29.81	G230L	5457	8244
J1503+6105	15 03 08.851	+61 05 51.69	G140L	600	9759
J1503-4152	15 03 33.929	-41 52 23.70	G140L	6000	8244
J1503-4152	15 03 33.929	-41 52 23.70	G230L	2457	8244
J1504+0122	15 04 50.171	+01 22 15.49	G140L	1320	9874
J1505+0342	15 05 56.561	+03 42 26.31	G140L	1320	9874
J1508+6717	15 08 40.411	+67 17 47.51	G140L	2448	7762
J1510+0058	15 10 24.932	+00 58 44.00	G140L	1320	9874
J1516+1900	15 16 53.240	+19 00 48.10	G140L	2857	9161
J1516+1900	15 16 53.240	+19 00 48.10	G230L	2311	9161
J1521-0009	15 21 01.974	-00 09 04.32	G230L	5236	9382

TABLE 1 — *Continued*

Object	R.A. (J2000)	DEC. (J2000)	Grating	Exp. (s)	Id
J1525+0026	15 25 10.598	+00 26 32.75	G230L	2387	9382
J1527+2452	15 27 01.761	+24 52 49.62	G230L	2200	9051
J1537+0021	15 37 13.740	+00 21 15.48	G230L	5232	9382
J1537+3358	15 37 31.022	+33 58 37.95	G230L	2236	9051
J1544+5912	15 44 20.101	+59 12 26.00	G140L	2139	8485
J1544+5912	15 44 20.101	+59 12 26.00	G230L	600	8485
J1554+0822	15 54 44.601	+08 22 22.00	G230L	900	9507
J1557-2029	15 57 21.200	-20 29 13.24	G230L	2321	8569
J1559-2442	15 59 41.418	-24 42 39.00	G230L	5057	8569
J1614+4859	16 14 26.810	+48 59 58.71	G140L	600	9759
J1614+4704	16 14 34.658	+47 04 20.31	G230L	2369	9051
J1619+3813	16 19 46.860	+38 13 28.81	G140L	1320	9874
J1631+4048	16 31 11.331	+40 48 05.11	G140L	1543	9506
J1631+1156	16 31 45.179	+11 56 03.17	G230L	2304	8569
J1636+7205	16 36 15.139	+72 05 12.73	G140L	1543	9506
J1637+2509	16 37 55.239	+25 09 30.58	G230L	2200	9051
J1649+3047	16 49 19.010	+30 47 18.00	G230L	49158	8266
J1649+3046	16 49 28.868	+30 46 52.40	G230L	27540	8266
J1701+6412	17 01 00.612	+64 12 09.90	G230L	2166	9982
J1701+6412	17 01 00.612	+64 12 09.90	G140L	2245	9982
J1702+6058	17 02 11.199	+60 58 50.00	G140L	3500	8024
J1702+6058	17 02 11.199	+60 58 50.00	G230L	700	8024
J1704+7057	17 04 26.104	+70 57 34.93	G230L	2691	8569
J1706+3615	17 06 34.109	+36 15 08.40	G230L	2268	9051
J1710+5923	17 10 14.517	+59 23 26.48	G230L	600	9759
J1711+6052	17 11 34.417	+60 52 40.48	G140L	600	9759
J1712+5559	17 12 44.092	+55 59 50.57	G230L	4380	9382
J1714+5757	17 14 13.411	+57 57 11.15	G230L	4380	9382
J1715+6453	17 15 30.498	+64 53 19.25	G140L	600	9759
J1715+4606	17 15 32.483	+46 06 40.19	G230L	2337	9051
J1715+5747	17 15 39.814	+57 47 22.03	G230L	4380	9382
J1716+5654	17 16 23.730	+56 54 45.26	G230L	9840	9382
J1717+5500	17 17 53.079	+55 00 47.98	G140L	600	9067
J1722+5442	17 22 37.031	+54 42 04.18	G230L	4380	9382
J1727+5302	17 27 38.943	+53 02 29.40	G230L	4380	9382
J1728-1415	17 28 19.797	-14 15 56.15	G140L	1140	8264
J1728-1415	17 28 19.797	-14 15 56.15	G230L	781	8264
J1729+7032	17 29 11.440	+70 32 58.78	G140L	720	9506
J1729+5758	17 29 58.799	+57 58 38.32	G230L	4380	9382
J1733+5533	17 33 23.064	+55 33 00.26	G230L	4380	9382
J1736+5938	17 36 44.253	+59 38 39.74	G230L	4380	9382
J1742+1827	17 42 06.958	+18 27 21.15	G140L	8138	8684
J1742+1827	17 42 06.958	+18 27 21.15	G230L	5267	8684
J1858+5645	18 58 26.917	+56 45 56.17	G230L	4260	8569
J1939+7007	19 39 29.407	+70 07 49.47	G140L	1344	9506
J1940-6907	19 40 25.569	-69 07 56.01	G140L	49924	7272
J1944+7705	19 44 54.902	+77 05 52.00	G140L	576	8582
J2006-0223	20 06 08.518	-02 23 35.09	G230L	2304	8569
J2051+1950	20 51 12.642	+19 50 06.99	G230L	2332	8569
J2114+0607	21 14 52.581	+06 07 42.92	G140L	1100	9277
J2114+0607	21 14 52.581	+06 07 42.92	G230L	900	9277
J2115-4323	21 15 06.877	-43 23 11.10	G230L	5315	7359
J2120-4426	21 20 11.609	-44 26 52.90	G230L	8279	7359
J2139-2454	21 39 13.271	-24 54 14.89	G230L	5057	8225
J2144-0754	21 44 32.717	-07 54 42.85	G230L	2110	9051
J2151+2130	21 51 45.828	+21 30 13.50	G230L	2333	8569
J2153-1514	21 53 19.138	-15 14 12.11	G140L	503	9858
J2154-4414	21 54 51.160	-44 14 05.85	G140L	720	9506
J2155-0922	21 55 01.531	-09 22 24.40	G230L	1667	9181
J2155-0922	21 55 01.531	-09 22 24.40	G140L	2640	9181
J2159-2417	21 59 24.961	-24 17 52.10	G230L	4738	8225
J2211-1705	22 11 15.417	-17 05 25.84	G230L	7904	7359
J2215-2944	22 15 16.040	-29 44 23.61	G230L	2376	8569
J2218-6150	22 18 51.042	-61 50 42.80	G140L	2520	8287
J2221-1857	22 21 39.492	-18 57 07.20	G140L	2312	8287
J2233-6033	22 33 37.668	-60 33 28.95	G230L	22124	7633
J2233-6033	22 33 37.668	-60 33 28.95	G140L	18480	8076
J2236+1343	22 36 07.690	+13 43 55.40	G230L	900	9507
J2252-5021	22 52 43.938	-50 21 37.71	G140L	2530	8287
J2253-3658	22 53 10.693	-36 58 15.70	G140L	2392	8287
J2255-5435	22 55 57.429	-54 35 26.20	G140L	2530	8287
J2258-2758	22 58 06.028	-27 58 21.15	G230L	2223	8225
J2304+0311	23 04 45.000	+03 11 46.00	G140L	2200	7358
J2316-2849	23 16 16.223	-28 49 00.20	G140L	2342	8287
J2316-3349	23 16 43.228	-33 49 12.30	G140L	2364	8287
J2328+0022	23 28 20.354	+00 22 37.09	G230L	5260	9382
J2330-5506	23 30 01.838	-55 06 23.57	G230L	900	9507

TABLE 1 — *Continued*

Object	R.A. (J2000)	DEC. (J2000)	Grating	Exp. (s)	Id
J2331+0038	23 31 21.804	+00 38 06.29	G230L	2379	9382
J2334+0052	23 34 39.983	+00 52 00.16	G230L	8157	9382
J2339-0029	23 39 17.827	-00 29 44.34	G230L	2347	9382
J2346-0016	23 46 25.671	-00 16 00.48	G140L	600	9067
J2350-4326	23 50 34.241	-43 26 00.00	G140L	2120	8875
J2350-4326	23 50 34.241	-43 26 00.00	G230L	1280	8875
J2351-1427	23 51 29.839	-14 27 56.80	G140L	2318	8287
J2352-0028	23 52 53.511	-00 28 51.31	G230L	2375	9382
J2353-0028	23 53 21.614	-00 28 41.66	G230L	2379	9382
J2358-5440	23 58 33.442	-54 40 42.21	G140L	2530	8287

TABLE 2  
OBSERVATIONS FROM FOS ARCHIVE (G160L)

Object	R.A. (J2000)	DEC. (J2000)	Exp. (s)	Id
preCOSTAR				
J0017+8135	00 17 08.563	+81 35 08.91	600	1027
J0017+8135	00 17 08.563	+81 35 08.91	25	1027
J0017+8135	00 17 08.563	+81 35 08.91	25	1027
J0027+2241	00 27 15.400	+22 41 58.50	1331	2424
J0047+0319	00 47 05.900	+03 19 54.90	530	2424
J0057-2643	00 57 58.012	-26 43 14.14	1200	3199
J0117-0841	01 17 23.338	-08 41 32.38	1127	3268
J0117-0841	01 17 23.338	-08 41 32.38	1143	4856
J0117-0841	01 17 23.338	-08 41 32.38	1143	4856
J0117-0841	01 17 23.338	-08 41 32.38	1143	4856
J0117-0841	01 17 23.338	-08 41 32.38	1143	4856
J0117-0841	01 17 23.338	-08 41 32.38	1143	4856
J0117-0841	01 17 23.338	-08 41 32.38	1143	4856
J0117-0841	01 17 23.338	-08 41 32.38	1143	4856
J0120+2133	01 20 17.250	+21 33 46.30	420	4396
J0145-0120	01 45 51.189	-01 20 30.73	50	1027
J0145-0120	01 45 51.189	-01 20 30.73	1200	1027
J0145-0120	01 45 51.189	-01 20 30.73	50	1027
J0148+3854	01 48 24.400	+38 54 04.00	420	4396
J0152-2001	01 52 27.291	-20 01 07.29	2000	3051
J0152-2001	01 52 27.291	-20 01 07.29	100	3051
J0152-2001	01 52 27.291	-20 01 07.29	2000	3051
J0152-2001	01 52 27.291	-20 01 07.29	2000	3051
J0156+0445	01 56 36.001	+04 45 28.47	1200	3199
J0235-0402	02 35 07.260	-04 02 05.80	1803	4799
J0256-0126	02 56 16.520	-01 26 37.40	360	4396
J0336-3607	03 36 09.280	-36 07 33.30	420	4396
J0351-1429	03 51 28.600	-14 29 09.10	530	2424
J0357-4812	03 57 21.900	-48 12 15.00	420	4396
J0448-2044	04 48 58.810	-20 44 45.70	480	4396
J0449-3911	04 49 42.299	-39 11 09.00	420	4396
J0745+3142	07 45 41.700	+31 42 55.70	563	3791
J0813+4813	08 13 36.059	+48 13 02.49	2172	3939
J0813+4813	08 13 36.059	+48 13 02.49	2172	3939
J0813+4813	08 13 36.059	+48 13 02.49	1200	1193
J0813+4813	08 13 36.059	+48 13 02.49	2173	3939
J0813+4813	08 13 36.059	+48 13 02.49	2172	3939
J0813+4813	08 13 36.061	+48 13 02.69	1620	5351
J0813+4813	08 13 36.061	+48 13 02.69	1580	5351
J0837+4450	08 37 52.745	+44 50 25.96	1400	3545
J0837+4450	08 37 52.745	+44 50 25.96	1400	3545
J0837+4450	08 37 52.745	+44 50 25.96	1400	3545
J0837+4450	08 37 52.745	+44 50 25.96	1400	3545
J0853+4349	08 53 34.200	+43 49 01.00	530	2424
J0859+4637	08 59 24.320	+46 37 17.39	480	4952
J0919+5106	09 19 57.700	+51 06 10.01	563	2424
J0949+2955	09 49 41.107	+29 55 19.12	100	3200
J0949+2955	09 49 41.107	+29 55 19.12	1768	3200
J1003+6813	10 03 06.801	+68 13 17.50	563	3791
J1010+4132	10 10 27.499	+41 32 39.10	563	3791
J1011+1304	10 11 10.800	+13 04 12.00	420	4952
J1024+1912	10 24 44.901	+19 12 19.60	1464	2424
J1041+0610	10 41 17.201	+06 10 16.60	1331	2424
J1042+1203	10 42 44.601	+12 03 31.30	1545	2424
J1058+1951	10 58 17.900	+19 51 51.00	1061	2424
J1107+1628	11 07 15.000	+16 28 02.40	563	3791
J1125+5910	11 25 53.851	+59 10 21.19	360	4952
J1126+3918	11 26 27.990	+39 18 44.79	360	4952
J1133+1052	11 33 30.300	+10 52 23.00	563	2424
J1139-1350	11 39 10.701	-13 50 43.10	530	2424
J1139+6547	11 39 57.100	+65 47 49.41	530	2424
J1208+4540	12 08 58.000	+45 40 36.00	530	2424
J1218+1105	12 18 26.100	+11 05 05.30	1677	2424
J1232-0224	12 32 00.000	-02 24 05.34	1000	1193
J1232-0224	12 32 00.088	-02 24 07.57	2029	3939
J1232-0224	12 32 00.088	-02 24 07.57	2029	3939
J1247+3209	12 47 20.801	+32 09 00.99	1331	2424
J1249-0559	12 49 13.843	-05 59 19.34	901	4081
J1254+1141	12 54 38.199	+11 41 06.10	853	2424
J1256+0427	12 56 59.901	+04 27 34.10	853	3791
J1308+3005	13 08 29.689	+30 05 39.00	480	4952
J1319+5148	13 19 46.230	+51 48 06.09	480	4953
J1319+2728	13 19 56.301	+27 28 08.40	798	2424
J1321+2847	13 21 14.736	+28 47 48.68	1000	1144
J1323+2910	13 23 20.581	+29 10 06.90	480	4953

TABLE 2 — *Continued*

Object	R.A. (J2000)	DEC. (J2000)	Exp. (s)	Id
J1331+3030	13 31 08.295	+30 30 32.86	900	1193
J1334+5501	13 34 11.660	+55 01 25.50	480	4953
J1336+1725	13 36 02.000	+17 25 13.00	530	2424
J1336-0048	13 36 47.131	-00 48 57.74	1127	3268
J1341+4123	13 41 00.798	+41 23 14.10	798	2424
J1343+2844	13 43 00.201	+28 44 08.00	1061	2424
J1349+5341	13 49 34.698	+53 41 17.40	1539	2424
J1351-0007	13 51 50.420	-00 07 39.70	480	4953
J1354+0052	13 54 58.700	+00 52 10.00	530	2424
J1357+1919	13 57 04.501	+19 19 06.60	530	2424
J1407+2827	14 07 00.399	+28 27 14.63	1530	6799
J1409+2618	14 09 23.877	+26 18 21.21	676	2424
J1418+1703	14 18 03.699	+17 03 24.90	1519	2424
J1427-1203	14 27 38.101	-12 03 49.90	563	2424
J1437-0147	14 37 48.259	-01 47 11.30	1450	6103
J1437-0147	14 37 48.259	-01 47 11.30	1510	6103
J1437-0147	14 37 48.270	-01 47 11.40	360	4953
J1445+0958	14 45 16.469	+09 58 36.12	1200	1027
J1445+0958	14 45 16.469	+09 58 36.12	50	1027
J1445+0958	14 45 16.469	+09 58 36.12	50	1027
J1524+0958	15 24 24.529	+09 58 29.46	1878	3200
J1524+0958	15 24 24.529	+09 58 29.46	1878	3200
J1524+0958	15 24 24.529	+09 58 29.46	100	3200
J1524+0958	15 24 24.529	+09 58 29.46	1878	3200
J1539+4735	15 39 34.794	+47 35 31.62	563	3791
J1620+1736	16 20 21.801	+17 36 24.00	563	2424
J1630+3758	16 30 13.586	+37 58 21.04	1000	1144
J1630+3756	16 30 20.815	+37 56 55.53	1000	1144
J1658+0515	16 58 33.501	+05 15 16.50	1061	2424
J1902+3159	19 02 56.082	+31 59 41.65	1460	6577
J2246-1206	22 46 18.201	-12 06 51.20	563	3791
J2253+1608	22 53 57.803	+16 08 53.40	530	2424
J2303-6807	23 03 43.499	-68 07 37.11	563	2424
J2342-0322	23 42 56.602	-03 22 26.50	563	4000
J2342-0322	23 42 56.602	-03 22 26.50	563	4000
J2342-0322	23 42 56.602	-03 22 26.50	516	4000
J2346+0930	23 46 36.899	+09 30 46.00	563	3791
J2355-3357	23 55 25.598	-33 57 55.80	563	2424

## COSTAR

J0102-2719	01 02 17.008	-27 19 50.06	1080	5455
J0102-2719	01 02 17.008	-27 19 50.06	300	5455
J0111+1753	01 11 49.793	+17 53 50.73	1350	5095
J0111+1753	01 11 49.793	+17 53 50.73	1350	5095
J0144+3411	01 44 11.780	+34 11 56.23	1580	6577
J0209-3939	02 09 28.570	-39 39 40.00	2220	6093
J0209-3939	02 09 28.570	-39 39 40.00	2500	6093
J0228-1011	02 28 39.150	-10 11 10.30	1360	5455
J0231+1322	02 31 45.910	+13 22 54.47	1400	6577
J0251+4315	02 51 34.590	+43 15 15.70	1660	6577
J0310-1909	03 10 28.079	-19 09 43.82	1270	5097
J0347+0105	03 47 40.200	+01 05 14.25	1490	6799
J0347+0105	03 47 40.200	+01 05 14.25	2430	6799
J0357-4812	03 57 21.870	-48 12 15.30	2570	6103
J0357-4812	03 57 21.870	-48 12 15.30	1650	6103
J0357-4812	03 57 21.870	-48 12 15.30	1220	6103
J0741+3111	07 41 10.681	+31 11 59.75	1520	6577
J0813+4813	08 13 36.061	+48 13 02.69	1620	5351
J0813+4813	08 13 36.061	+48 13 02.69	1580	5351
J0830+2410	08 30 52.101	+24 10 59.45	1560	6577
J0845+3420	08 45 38.661	+34 20 43.30	1680	6091
J0845+1328	08 45 47.271	+13 28 58.41	1540	6577
J0906+1722	09 06 38.214	+17 22 23.16	450	5455
J0906+1722	09 06 38.214	+17 22 23.16	870	5455
J0935+4953	09 35 53.009	+49 53 13.79	1440	6314
J0935+4953	09 35 53.130	+49 53 13.60	1200	5455
J0954+1743	09 54 56.851	+17 43 31.09	1430	6577
J1001+5553	10 01 20.739	+55 53 55.10	240	5683
J1001+5553	10 01 20.889	+55 53 49.20	240	5683
J1001+5454	10 01 29.722	+54 54 38.13	1670	6577
J1038-2752	10 38 08.434	-27 52 37.99	1510	6577
J1052+6125	10 52 32.849	+61 25 20.56	1660	6577
J1130-1449	11 30 07.020	-14 49 27.60	1450	6577
J1150-0023	11 50 43.861	-00 23 55.10	1260	5095
J1150-0023	11 50 43.861	-00 23 55.10	1040	5095
J1151+3825	11 51 29.290	+38 25 53.04	1520	6577

TABLE 2 — *Continued*

Object	R.A. (J2000)	DEC. (J2000)	Exp. (s)	Id
J1211+1030	12 11 40.620	+10 30 02.50	1940	5351
J1211+1030	12 11 40.620	+10 30 02.50	1260	5351
J1256+5652	12 56 14.216	+56 52 25.08	770	6799
J1311-0552	13 11 36.486	-05 52 38.95	450	5455
J1311-0552	13 11 36.486	-05 52 38.95	930	5455
J1407+2827	14 07 00.399	+28 27 14.63	1530	6799
J1415+1129	14 15 46.300	+11 29 44.10	960	5455
J1437-0147	14 37 48.259	-01 47 11.30	1450	6103
J1437-0147	14 37 48.259	-01 47 11.30	1510	6103
J1513+1011	15 13 29.330	+10 11 05.87	1550	6577
J1601+1714	16 01 20.350	+17 14 15.75	2340	5095
J1601+1714	16 01 20.350	+17 14 15.75	1280	5095
J1625+2646	16 25 48.907	+26 46 58.76	1920	6577
J1716+5328	17 16 35.310	+53 28 15.27	1660	6577
J1902+3159	19 02 56.082	+31 59 41.65	1460	6577
J2124-1744	21 24 41.660	-17 44 45.90	1470	6799
J2124-1744	21 24 41.660	-17 44 45.90	2420	6799

TABLE 3  
LIST OF OBJECTS USED IN SAMPLE R1/R2.

Object <sup>a</sup>	$z_{\text{em}}$	R1 <sup>b</sup>		R2 <sup>c</sup>	
		$z_{\text{min}}$	$z_{\text{max}}$	$z_{\text{min}}$	$z_{\text{max}}$
J0001+0709	3.234	2.226	2.481	2.214	2.481
B0002+0507	1.900	1.470	1.871	1.470	1.871
B0002-4214	2.760	2.301	2.594	2.301	2.594
B0003+1553	0.450	0.330	0.435	0.289	0.435
J0012-0122	1.998	1.387	1.968	1.387	1.968
J0021+0043	1.243	0.943	1.221	0.943	1.221
J0021+0104	1.829	1.575	1.801	1.575	1.801
J0021-0128A	1.588	1.403	1.562	1.243	1.562
J0022-0128B	1.040	0.830	1.020	0.830	1.020
J0027+2241	1.108	0.542	1.087	0.497	1.087
J0038-3501	1.199	0.852	1.177	0.813	1.177
J0038-3504	1.519	0.964	1.494	0.759	1.494
J0039-3529	1.095	0.813	1.074	0.797	1.074
J0043-2622	3.053	1.880	2.478	1.880	2.478
J0047+0319	0.624	...	...	0.495	0.608
J0051+0041	1.188	0.995	1.166	0.870	1.166
B0058+0155	1.954	1.035	1.535	0.824	1.535
J0102-0853	1.682	1.178	1.655	1.178	1.655
J0106+0105	1.611	1.293	1.585	1.293	1.585
B0107-0235	0.948	0.793	0.929	0.780	0.929
J0116-0043	1.263	0.915	1.240	0.915	1.240
B0119-0437	1.925	1.470	1.896	1.470	1.896
J0120+2133	1.500	1.318	1.475	1.050	1.475
B0122-0021	1.070	0.820	1.049	0.791	1.049
J0123-0058	1.550	1.397	1.524	1.397	1.524
J0126-0105	1.609	1.193	1.583	1.193	1.583
J0128-3029	0.475	0.255	0.460	0.255	0.460
J0134+0051	1.522	1.348	1.497	1.268	1.497
J0137-2430	0.831	0.790	0.813	0.738	0.813
J0138-0005	1.340	1.219	1.317	1.112	1.317
J0139-0023	1.384	1.082	1.360	1.082	1.360
J0141-0024	2.611	2.215	2.464	2.215	2.464
B0143-0135	3.124	1.612	2.593	1.612	2.593
J0144+3411	1.450	0.765	1.385	0.765	1.390
J0148+3854	1.442	...	...	1.215	1.418
B0150-2015	2.139	1.474	2.108	1.474	2.108
J0152-2001	2.147	1.447	1.658	1.447	1.658
J0153+0009	0.837	0.793	0.819	0.793	0.819
J0153+0052	1.163	1.053	1.141	1.053	1.141
J0157-0048	1.545	1.411	1.520	1.411	1.520
B0207-3953	2.813	2.480	2.593	2.480	2.593
J0208-0503	1.850	1.072	1.822	1.072	1.822
B0219+4248	0.444	...	...	0.331	0.430
J0235-0402	1.438	0.497	1.414	0.497	1.414
J0240-1851	0.631	0.257	0.615	0.242	0.615
J0241-1514	2.786	...	...	2.198	2.474
J0251+4315	1.310	0.871	1.287	0.771	1.287
B0254-3327b	1.915	1.583	1.886	1.474	1.886
J0256-0126	0.879	0.814	0.860	0.814	0.860
J0304-0008	3.290	2.112	2.476	0.919	2.476
J0318-2012	2.869	...	...	2.084	2.473
J0336-3607	1.093	...	...	0.871	1.072
J0351-1429	0.614	0.487	0.598	0.487	0.598
J0354-2724	2.823	...	...	1.858	2.474
J0357-4812	1.016	0.511	0.996	0.504	0.996
J0411-4956	0.817	0.785	0.799	0.785	0.799
B0421+0157	2.044	1.473	2.014	1.473	2.014
J0423-0120	0.915	0.839	0.896	0.805	0.896
B0424-1309	2.159	2.036	2.127	2.036	2.127
J0436-5258	1.231	0.263	0.881	0.259	0.881
J0439-2422	0.840	0.819	0.822	0.754	0.822
J0440-5248	1.053	0.264	0.881	0.261	0.881
J0441-4313	0.593	0.262	0.577	0.259	0.577
J0448-2044	1.896	1.457	1.740	0.580	1.746
J0452-1640	2.600	1.008	2.474	1.008	2.474
J0453-1305	2.300	2.068	2.267	2.068	2.267
B0453-4220	2.660	2.303	2.593	2.303	2.593
B0454+0356	1.345	0.858	1.322	0.858	1.322
B0454-2203	0.534	0.473	0.519	0.473	0.519
J0504-2944	0.552	0.256	0.536	0.255	0.536
J0514-3326	1.569	1.131	1.543	1.131	1.543
B0624+6907	0.374	0.329	0.360	0.311	0.360
J0741+3111	0.630	0.482	0.614	0.482	0.614
J0806+5041	2.432	1.101	2.398	1.079	2.398

TABLE 3 — *Continued*

Object <sup>a</sup>	$z_{\text{em}}$	R1 <sup>b</sup>		R2 <sup>c</sup>	
		$z_{\text{min}}$	$z_{\text{max}}$	$z_{\text{min}}$	$z_{\text{max}}$
J0830+2410	0.939	0.772	0.920	0.772	0.920
J0839+5256	1.545	0.328	0.882	0.328	0.882
J0845+1328	1.877	0.768	1.254	0.768	1.357
J0853+4349	0.513	...	...	0.495	0.498
J0859+4637	0.923	0.615	0.904	0.499	0.904
J0912+2450	0.654	0.262	0.637	0.259	0.637
J0919+5106	0.553	0.512	0.537	0.495	0.537
B0933+7315	2.528	2.332	2.493	2.332	2.493
B0935+4141	1.937	1.465	1.908	1.465	1.908
J0944+2554	2.910	2.235	2.456	2.235	2.456
J0948+4323	1.892	1.227	1.863	1.227	1.863
B0953+5454	2.584	2.510	2.548	2.510	2.548
J0953-0038	1.382	1.016	1.358	1.016	1.358
J0954+1743	1.478	0.502	1.453	0.502	1.453
B0954+5537	0.909	0.844	0.890	0.803	0.890
B0955+3238	0.533	...	...	0.331	0.518
J0958+3224	0.530	0.258	0.515	0.256	0.515
B1001+2910	0.329	0.286	0.316	0.286	0.316
J1003+6813	0.773	0.705	0.755	0.505	0.755
J1008-0018	1.350	0.931	1.327	0.876	1.327
J1009+0036	1.702	1.031	1.675	0.959	1.675
J1009-0026	1.244	0.889	1.222	0.889	1.222
J1010+0003	1.399	1.266	1.375	1.266	1.375
J1010+4132	0.613	0.495	0.597	0.495	0.597
J1010-0047	1.671	1.328	1.644	1.328	1.644
J1011+1304	1.287	0.879	1.264	0.497	1.264
B1017+2759	1.928	1.502	1.899	1.473	1.899
J1017+5356	1.400	1.296	1.376	1.296	1.376
J1022+0101	1.563	...	...	1.416	1.537
J1022+3041	1.318	0.345	0.882	0.310	0.882
J1024+1912	0.828	0.745	0.810	0.530	0.810
J1028-0100	1.530	0.843	1.505	0.801	1.505
J1032+0003	1.190	1.106	1.168	1.106	1.168
J1037+0028	1.733	1.425	1.706	1.425	1.706
J1038-2752	2.168	0.833	1.028	0.825	1.259
J1041+0610	1.265	0.514	1.242	0.502	1.242
J1042+1203	1.028	0.714	1.008	0.619	1.008
B1047+5503	2.165	1.637	2.133	1.464	2.133
J1048+0032	1.649	1.194	1.623	1.194	1.623
J1054-0020	1.021	...	...	0.952	1.001
J1058+1951	1.110	1.037	1.089	1.037	1.089
B1100+7715	0.311	...	...	0.283	0.298
B1100-2629	2.145	1.838	2.114	1.838	2.114
J1103+3715	1.295	1.239	1.272	1.239	1.272
B1104-1805a	2.303	1.662	2.270	1.662	2.270
J1107+0048	1.391	0.919	1.367	0.831	1.367
J1107+1628	0.632	0.483	0.616	0.483	0.616
J1108+3133	2.244	1.194	2.212	1.194	2.212
J1109+0051	0.957	0.834	0.937	0.803	0.937
J1110+3019	1.521	1.245	1.496	1.085	1.496
B1115+0802a2	1.722	1.471	1.695	1.471	1.695
J1125+5910	0.852	0.259	0.833	0.259	0.833
J1130-1449	1.187	0.502	1.165	0.502	1.165
J1139-1350	0.554	...	...	0.497	0.538
J1143+3452	3.130	0.556	0.880	0.556	0.880
B1146+1103e	1.100	0.813	1.079	0.795	1.079
B1146+1104b	1.010	0.852	0.990	0.820	0.990
B1148+5454	0.978	0.360	0.958	0.330	0.958
J1150-0023	1.980	0.502	1.751	0.502	1.751
J1151+3825	1.304	0.544	1.281	0.489	1.281
J1208+4540	1.155	0.767	1.133	0.502	1.133
J1211+1030	2.193	0.698	1.751	0.636	1.751
B1216+0655	0.334	0.309	0.321	0.284	0.321
J1218+1105	1.403	1.080	1.379	0.572	1.379
J1220+3343	1.532	1.502	1.507	1.415	1.507
J1220-0040	1.411	0.963	1.387	0.963	1.387
B1222+2251	2.046	1.174	1.535	1.174	1.535
J1224+0037	1.482	1.268	1.457	1.268	1.457
J1225+0035	1.226	1.099	1.204	1.038	1.204
B1225+3145	2.219	1.796	2.187	1.796	2.187
J1225-0052	0.964	0.910	0.944	0.844	0.944
J1226-0006	1.118	...	...	1.077	1.097
J1228+1018	2.305	1.392	2.272	1.126	2.272
J1232-0224	1.038	0.761	1.018	0.485	1.018
B1247+2647	2.043	1.470	2.013	1.470	2.013

TABLE 3 — *Continued*

Object <sup>a</sup>	$z_{\text{em}}$	R1 <sup>b</sup>		R2 <sup>c</sup>	
		$z_{\text{min}}$	$z_{\text{max}}$	$z_{\text{min}}$	$z_{\text{max}}$
J1247+3209	0.949	0.756	0.930	0.500	0.930
B1248+3142	1.020	0.782	1.000	0.771	1.000
B1248+4007	1.030	0.773	1.010	0.773	1.010
B1249+2929	0.820	0.775	0.802	0.775	0.802
J1254+1141	0.870	0.570	0.851	0.500	0.851
B1259+5918	0.472	0.297	0.457	0.280	0.457
J1313-2716	2.186	1.684	2.154	1.684	2.154
J1319+2728	1.014	0.661	0.994	0.661	0.994
J1319+5148	1.055	0.687	1.034	0.500	1.034
B1320+2925	0.960	0.841	0.940	0.794	0.940
J1321+1106	2.181	1.971	2.149	1.849	2.149
J1321+2847	1.703	1.135	1.676	1.135	1.676
J1322+4739	1.554	1.072	1.528	1.072	1.528
J1322+4739	1.101	0.921	1.080	0.753	1.080
J1323-0021	1.388	1.331	1.364	1.085	1.364
B1328+3045	0.849	0.790	0.831	0.780	0.831
B1329+4117	1.930	1.283	1.901	1.283	1.901
J1331+3030	0.846	0.701	0.828	0.701	0.828
B1334-0033	2.783	0.803	2.594	0.552	2.594
J1336+1725	0.554	0.502	0.538	0.502	0.538
J1341+0059	1.714	1.597	1.687	1.597	1.687
J1341+4123	1.204	0.683	1.182	0.502	1.182
J1342+6021	0.961	0.258	0.941	0.258	0.941
J1343+2844	0.905	0.704	0.886	0.499	0.886
J1345-0023	1.095	0.811	1.074	0.784	1.074
J1351-0007	1.444	1.159	1.420	1.159	1.420
J1354+0052	1.121	0.667	1.100	0.667	1.100
J1357+1919	0.719	0.608	0.702	0.497	0.702
J1404-0130	2.522	1.719	2.482	1.719	2.482
J1409+2618	0.945	0.502	0.926	0.502	0.926
J1418+1703	0.821	0.725	0.803	0.495	0.803
J1419-0036	0.969	0.822	0.949	0.822	0.949
J1420-0054	1.458	1.332	1.433	1.332	1.433
J1423+3252	1.905	1.490	1.876	1.176	1.876
J1426+0051	1.333	0.940	1.310	0.838	1.310
J1427-1203	0.805	...	...	0.652	0.787
J1431+3952	1.215	0.823	1.193	0.803	1.193
J1431-0050	1.188	0.942	1.166	0.858	1.166
B1435+6349	2.068	1.938	2.037	1.938	2.037
J1436-0051	1.273	1.109	1.250	0.919	1.250
J1437-0147	1.310	0.499	1.287	0.499	1.287
J1455-0045	1.375	1.095	1.351	1.095	1.351
J1501+0019	1.930	1.486	1.901	1.486	1.901
J1502-4154	1.026	...	...	1.001	1.006
J1504+0122	0.967	0.271	0.882	0.259	0.882
J1513+1011	1.546	1.042	1.521	1.042	1.521
B1517+2356	1.903	1.725	1.874	0.820	1.874
B1517+2357	1.834	0.821	1.806	0.800	1.806
J1521-0009	1.318	1.094	1.295	0.955	1.295
J1524+0958	1.324	0.501	1.301	0.501	1.301
J1527+2452	0.993	...	...	0.946	0.973
J1537+0021	1.754	1.632	1.726	1.632	1.726
J1537+3358	1.025	0.902	1.005	0.902	1.005
J1539+4735	0.772	0.715	0.754	0.520	0.754
B1542+5408	2.371	0.996	2.337	0.996	2.337
B1544+4855	0.400	0.331	0.386	0.322	0.386
J1544+5912	0.807	0.260	0.789	0.259	0.789
J1601+1714	1.952	1.581	1.736	1.538	1.751
J1614+4704	1.860	1.405	1.831	1.405	1.831
J1619+3813	1.124	0.258	0.883	0.258	0.883
J1620+1736	0.555	0.535	0.539	0.488	0.539
B1622+2352	0.927	0.891	0.908	0.891	0.908
B1623+2653	2.526	1.042	2.491	1.042	2.491
J1629+3808	1.461	1.110	1.436	0.981	1.436
J1631+1156	1.792	1.112	1.764	0.974	1.764
J1637+2509	1.110	0.999	1.089	0.888	1.089
J1649+3046	1.123	1.072	1.102	1.072	1.102
J1658+0515	0.879	0.539	0.860	0.499	0.860
B1704+6048	0.371	0.312	0.357	0.283	0.357
J1704+7057	2.015	1.810	1.985	1.029	1.985
J1706+3615	0.918	0.826	0.899	0.794	0.899
J1712+5559	1.358	1.209	1.334	1.209	1.334
B1715+5331	1.940	1.470	1.911	1.470	1.911
J1716+5654	0.937	...	...	0.905	0.918
B1718+4807	1.084	0.776	1.063	0.776	1.063

TABLE 3 — *Continued*

Object <sup>a</sup>	$z_{\text{em}}$	R1 <sup>b</sup>		R2 <sup>c</sup>	
		$z_{\text{min}}$	$z_{\text{max}}$	$z_{\text{min}}$	$z_{\text{max}}$
J1722+5442	1.215	0.948	1.193	0.864	1.193
J1727+5302	1.444	1.032	1.420	1.032	1.420
J1729+5758	1.342	0.856	1.319	0.824	1.319
J1733+5533	1.072	0.999	1.051	0.999	1.051
B1821+1042	1.360	1.252	1.336	1.252	1.336
J1858+5645	1.595	1.234	1.569	1.234	1.569
J1902+3159	0.635	0.482	0.619	0.482	0.619
J2051+1950	2.367	1.833	2.333	1.747	2.333
B2145+0643	0.999	0.820	0.979	0.802	0.979
J2151+2130	1.534	1.170	1.509	1.004	1.509
J2154-4414	0.344	0.256	0.331	0.256	0.331
J2215-2944	2.706	0.936	2.594	0.862	2.594
B2216-0350	0.901	...	...	0.862	0.882
J2233-6033	2.238	0.265	2.206	0.263	2.206
J2246-1206	0.630	0.499	0.614	0.499	0.614
J2253+1608	0.859	0.793	0.840	0.537	0.840
J2258-2758	0.927	0.819	0.908	0.790	0.908
J2328+0022	1.308	0.836	1.285	0.809	1.285
J2331+0038	1.486	1.143	1.461	1.143	1.461
J2334+0052	1.040	0.854	1.020	0.823	1.020
J2339-0029	1.340	...	...	1.155	1.317
J2342-0322	0.896	0.539	0.877	0.499	0.877
J2346+0930	0.673	0.614	0.656	0.499	0.656
J2352-0028	1.624	1.345	1.598	1.318	1.598
J2355-3357	0.702	0.497	0.685	0.486	0.685

<sup>a</sup> Objects with a B preface designate objects listed with coordinates from the Besselian epoch (1950). These objects were observed with the FOS high resolution gratings and can be found in Bechtold et al. (2002). Objects with a J preface designate objects listed with coordinates from the Julian epoch (2000). These objects were observed with either the FOS low resolution gratings or the

STIS low resolution gratings described in § 3 and listed in Table 1 and Table 2.

<sup>b</sup>  $\tau \geq 1$

<sup>c</sup>  $\tau \geq 2$

TABLE 4  
LIST OF LLSs.

Object <sup>a</sup>	$z_{\text{em}}$	$z_{\text{LLS}}^{\text{b}}$	$\tau_{\text{LLS}}$	$\log N_{\text{HI}}$	Sample <sup>c</sup>	Instrument <sup>d</sup>
B0002-4214	2.760	2.301	$> 4.06$	$> 17.81$	R1,R2	FOS-H
J0012-0122	1.998	1.727	$1.70 \pm 0.08$	$17.44^{+0.01}_{-0.02}$	R1	STIS
J0012-0122	1.998	1.387	$> 2.33$	$> 17.57$	MgII	STIS
J0021+0043	1.243	0.943	$> 2.97$	$> 17.67$	MgII	STIS
J0021+0104	1.829	1.576	$> 2.47$	$> 17.59$	MgII	STIS
J0021-0128A	1.588	1.499	$0.96 \pm 0.07$	$17.19^{+0.03}_{-0.04}$	PLLS	STIS
J0021-0128A	1.588	1.409	$1.16 \pm 0.13$	$17.27^{+0.04}_{-0.06}$	R1	STIS
J0021-0128A	1.588	1.243	$> 2.01$	$> 17.50$	R2	STIS
J0038-3504	1.519	1.517	$0.87 \pm 0.04$	$17.14^{+0.02}_{-0.02}$	PLLS,Prox	STIS
J0038-3504	1.519	1.114	$0.22 \pm 0.08$	$16.55^{+0.14}_{-0.20}$	PLLS	STIS
J0039-3528	0.836	0.838	$> 1.84$	$> 17.47$	Prox	STIS
J0043-2622	3.053	1.880	$1.38 \pm 0.15$	$17.34^{+0.05}_{-0.05}$	R1	STIS
J0043-2622	3.053	1.384	$> 1.71$	$> 17.43$	LQ	STIS
B0058+0155	1.954	1.463	$0.77 \pm 0.05$	$17.09^{+0.03}_{-0.03}$	PLLS	FOS-H
J0102-0853	1.682	1.185	$> 2.49$	$> 17.60$	R1,R2	STIS
J0106+0105	1.611	1.356	$> 2.68$	$> 17.63$	MgII	STIS
J0109-2307	0.818	0.821	$> 1.72$	$> 17.44$	Prox	STIS
J0116-0043	1.263	0.915	$> 1.89$	$> 17.48$	MgII	STIS
B0119-0437	1.925	1.964	$1.81 \pm 0.04$	$17.46^{+0.01}_{-0.01}$	Prox	FOS-H
J0120+2133	1.500	1.327	$1.58 \pm 0.06$	$17.40^{+0.02}_{-0.01}$	R1	FOS-L
J0120+2133	1.500	1.050	$2.61 \pm 0.31$	$17.62^{+0.05}_{-0.05}$	R2	FOS-L
J0123-0058	1.550	1.412	$> 2.79$	$> 17.65$	MgII	STIS
J0126-0105	1.609	1.193	$> 2.73$	$> 17.64$	MgII	STIS
J0134+0051	1.522	1.449	$1.07 \pm 0.09$	$17.23^{+0.04}_{-0.04}$	R1	STIS
J0134+0051	1.522	1.274	$> 1.81$	$> 17.46$	LQ	STIS
J0138-0005	1.340	1.342	$0.64 \pm 0.10$	$17.01^{+0.06}_{-0.07}$	PLLS,Prox	STIS
J0139-0023	1.384	1.089	$1.65 \pm 0.22$	$17.42^{+0.06}_{-0.06}$	R1	STIS
J0141-0024	2.611	2.215 <sup>b</sup>	$> 2.95$	$> 17.67$	R1,R2	STIS
B0143-0135	3.124	1.612	$> 2.59$	$> 17.61$	R1,R2	FOS-H
J0144+3411	1.450	1.243	$1.82 \pm 0.07$	$17.46^{+0.02}_{-0.01}$	MgII	FOS-L
J0148+3854	1.442	1.215 <sup>b</sup>	$> 2.66$	$> 17.62$	R2	FOS-L
J0153+0009	0.837	0.773	.....	.....	MgII,Blue	STIS
J0153+0052	1.163	1.062	$> 2.80$	$> 17.65$	MgII	STIS
J0157-0048	1.545	1.417	$> 3.76$	$> 17.78$	MgII	STIS
B0207-3953	2.813	2.480	$> 3.33$	$> 17.72$	R1,R2	FOS-H
J0208-0503	1.850	1.072	$> 1.80$	$> 17.46$	DLA	STIS
J0210-0152	2.370	2.381	$1.29 \pm 0.38$	$17.31^{+0.12}_{-0.15}$	LQ,Prox	STIS
J0210-0152	2.370	2.147	$> 1.66$	$> 17.42$	LQ	STIS
J0241-1514	2.786	2.198	$1.45 \pm 0.32$	$17.36^{+0.09}_{-0.10}$	LQ	STIS
J0241-1514	2.786	1.839 <sup>b</sup>	$> 2.11$	$> 17.52$	LQ	STIS
J0256-0126	0.879	0.814 <sup>b</sup>	$> 3.43$	$> 17.74$	R1,R2	FOS-L
J0304-0008	3.290	2.112	$0.79 \pm 0.09$	$17.10^{+0.05}_{-0.05}$	PLLS	STIS
J0304-0008	3.290	1.985	$0.72 \pm 0.11$	$17.06^{+0.06}_{-0.07}$	PLLS	STIS
J0318-2012	2.869	2.090	$> 2.83$	$> 17.65$	R2	STIS
J0336-3607	1.093	0.871 <sup>b</sup>	$> 2.14$	$> 17.53$	R2	FOS-L
J0354-2724	2.823	1.858 <sup>b</sup>	$> 2.51$	$> 17.60$	R2	STIS
J0411-4956	0.817	0.785	$> 1.25$	$> 17.30$	R1	STIS
B0424-1309	2.159	2.036	$> 3.91$	$> 17.79$	R1,R2	FOS-H
J0452-1640	2.600	1.008	$> 2.11$	$> 17.52$	MgII	STIS
J0453-1305	2.300	2.068	$> 4.28$	$> 17.83$	R1,R2	STIS
B0453-4220	2.660	2.304	$> 4.08$	$> 17.81$	R1,R2	FOS-H
B0454+0356	1.345	1.153	$1.13 \pm 0.04$	$17.26^{+0.01}_{-0.02}$	R1	FOS-H
B0454+0356	1.345	0.993	$0.68 \pm 0.04$	$17.04^{+0.02}_{-0.03}$	PLLS	FOS-H
B0454+0356	1.345	0.858	$> 2.41$	$> 17.58$	R1,R2	FOS-H
B0454-2203	0.534	0.473	$> 3.43$	$> 17.74$	R1,R2	FOS-H
J0514-3326	1.569	1.138	$> 3.73$	$> 17.77$	R1,R2	STIS
J0514-3326	1.569	0.935	.....	.....	Blue	STIS
J0806+5041	2.432	1.814	$0.80 \pm 0.05$	$17.10^{+0.03}_{-0.02}$	PLLS	STIS
J0806+5041	2.432	1.677	$0.68 \pm 0.06$	$17.04^{+0.03}_{-0.04}$	PLLS	STIS
J0806+5041	2.432	1.322	$0.71 \pm 0.09$	$17.06^{+0.05}_{-0.07}$	PLLS	STIS
J0806+5041	2.432	1.065	$0.50 \pm 0.19$	$16.90^{+0.15}_{-0.21}$	PLLS	STIS
J0813+4813	0.871	0.866	$> 2.11$	$> 17.52$	Prox,21cm	FOS-L
J0839+5256	1.545	0.328	$1.21 \pm 0.27$	$17.29^{+0.09}_{-0.11}$	R1	STIS
B0848+1623	1.936	1.926	$> 4.71$	$> 17.87$	Prox	FOS-H
J0912+2450	0.654	0.376	$0.50 \pm 0.05$	$16.90^{+0.04}_{-0.04}$	PLLS	STIS
B0933+7315	2.528	2.332	$> 4.00$	$> 17.80$	R1,R2	FOS-H
B0933+7315	2.528	1.508 <sup>b</sup>	$> 1.67$	$> 17.42$	LQ	FOS-H

TABLE 4 — *Continued*

Object <sup>a</sup>	$z_{\text{em}}$	$z_{\text{LLS}}^{\text{b}}$	$\tau_{\text{LLS}}$	$\log N_{\text{HI}}$	Sample <sup>c</sup>	Instrument <sup>d</sup>
B0935+4141	1.937	1.465	> 4.81	> 17.88	R1,R2	FOS-H
J0944+2554	2.910	2.235	> 2.98	> 17.67	R1,R2	STIS
J0944+2554	2.910	1.466	$1.33 \pm 0.32$	$17.33^{+0.09}_{-0.12}$	LQ	STIS
J0948+4323	1.892	1.235	> 3.00	> 17.68	DLA	STIS
B0953+5454	2.584	2.510 <sup>b</sup>	> 4.00	> 17.80	R1,R2	FOS-H
J0953-0038	1.382	1.016	> 2.30	> 17.56	R1,R2	STIS
B0958+5509	1.750	1.733	> 5.31	> 17.93	Prox	FOS-H
J1001+5553A	1.413	1.392	> 4.57	> 17.86	Prox	STIS
J1001+5553B	1.413	1.392	> 4.68	> 17.87	Prox,GL	STIS
J1008-0018	1.350	1.196	$1.13 \pm 0.06$	$17.26^{+0.02}_{-0.03}$	R1	STIS
J1009+0036	1.702	0.973	> 2.17	> 17.54	MgII	STIS
J1009-0026	1.244	1.145	$0.48 \pm 0.08$	$16.88^{+0.07}_{-0.08}$	PLLS	STIS
J1009-0026	1.244	1.118	$0.33 \pm 0.07$	$16.72^{+0.08}_{-0.11}$	PLLS	STIS
J1009-0026	1.244	0.889	> 1.87	> 17.47	MgII	STIS
J1009-0026	1.244	0.843	.....	.....	MgII,Blue	STIS
J1010+0003	1.399	1.266	> 3.12	> 17.69	MgII	STIS
J1010-0047	1.671	1.328	> 3.58	> 17.75	MgII	STIS
J1011+1304	1.287	0.900	$1.36 \pm 0.11$	$17.34^{+0.03}_{-0.04}$	R1	FOS-L
B1017+2759	1.928	1.608	$1.52 \pm 0.05$	$17.39^{+0.01}_{-0.02}$	R1	FOS-H
J1017+5356	1.400	1.307	> 3.13	> 17.69	DLA	STIS
J1022+0101	1.563	1.560	$2.09 \pm 0.11$	$17.52^{+0.03}_{-0.02}$	Prox	STIS
J1022+0101	1.563	1.427	> 1.89	> 17.48	MgII	STIS
J1022+3041	1.318	0.435	$0.41 \pm 0.08$	$16.82^{+0.07}_{-0.10}$	PLLS	STIS
J1022+3041	1.318	0.346	$2.40 \pm 0.31$	$17.58^{+0.06}_{-0.06}$	DLA	STIS
J1024+1912	0.828	0.530 <sup>b</sup>	> 2.23	> 17.55	R2	FOS-L
J1032+0003	1.190	1.105	> 2.72	> 17.63	MgII	STIS
J1037+0028	1.733	1.425	> 2.97	> 17.67	MgII	STIS
J1042+1203	1.028	0.661	$0.57 \pm 0.13$	$16.96^{+0.09}_{-0.11}$	PLLS	FOS-L
B1047+5503	2.165	1.637	$0.84 \pm 0.05$	$17.13^{+0.03}_{-0.03}$	PLLS	FOS-H
J1048+0032	1.649	1.194	> 2.61	> 17.62	R1,R2	STIS
J1054-0020	1.021	0.952	> 1.61	> 17.41	MgII	STIS
J1058+1951	1.110	1.037	$2.22 \pm 0.13$	$17.55^{+0.03}_{-0.02}$	R1,R2	FOS-L
B1100-2629	2.145	1.838	> 5.42	> 17.93	R1,R2	FOS-H
J1103+3715	1.295	1.246	> 2.15	> 17.53	R1,R2	STIS
B1103+6416	2.190	1.892	$1.81 \pm 0.03$	$17.46^{+0.01}_{-0.00}$	IUE	FOS-H
B1103+6416	2.190	0.976	$0.34 \pm 0.07$	$16.73^{+0.09}_{-0.10}$	IUE	FOS-H
B1104-1805a	2.303	2.201	$0.20 \pm 0.03$	$16.51^{+0.06}_{-0.09}$	PLLS	FOS-H
B1104-1805a	2.303	1.662	> 4.55	> 17.86	DLA	FOS-H
B1104-1805b	2.303	2.201	$0.60 \pm 0.04$	$16.98^{+0.03}_{-0.03}$	PLLS	FOS-H
B1104-1805b	2.303	1.662	$1.99 \pm 0.21$	$17.50^{+0.05}_{-0.05}$	DLA	FOS-H
J1107+0048	1.391	1.082	$1.03 \pm 0.06$	$17.22^{+0.02}_{-0.03}$	MgII	STIS
J1108+3133	2.244	2.106	$1.50 \pm 0.07$	$17.38^{+0.02}_{-0.02}$	R1	STIS
J1108+3133	2.244	1.200	> 2.11	> 17.52	R1,R2	STIS
J1110+3019	1.521	1.030	> 1.64	> 17.41	DLA	STIS
J1112+0013	1.433	1.423	> 2.53	> 17.60	Prox	STIS
J1125+5910	0.852	0.558	$0.33 \pm 0.05$	$16.72^{+0.06}_{-0.06}$	PLLS	STIS
J1126+0034	1.783	1.793	> 3.49	> 17.74	Prox	STIS
J1143+3452	3.130	0.556 <sup>b</sup>	> 4.48	> 17.85	R1,R2	STIS
J1150-0023	1.980	1.446	$0.95 \pm 0.05$	$17.18^{+0.02}_{-0.03}$	PLLS	FOS-L
J1151+3825	1.304	0.548	$1.69 \pm 0.12$	$17.43^{+0.03}_{-0.03}$	MgII	FOS-L
J1208+4540	1.158	0.928	$0.79 \pm 0.06$	$17.10^{+0.03}_{-0.04}$	PLLS	FOS-L
J1218+1105	1.403	1.266	$0.66 \pm 0.06$	$17.02^{+0.04}_{-0.04}$	PLLS	FOS-L
J1218+1105	1.403	1.110	$0.74 \pm 0.08$	$17.07^{+0.05}_{-0.04}$	PLLS	FOS-L
J1220+3343	1.532	1.502	$1.85 \pm 0.13$	$17.47^{+0.03}_{-0.03}$	R1	STIS
J1220-0040	1.411	0.976	> 1.97	> 17.49	MgII	STIS
B1222+2251	2.046	1.174	$0.71 \pm 0.13$	$17.05^{+0.08}_{-0.08}$	PLLS	FOS-H
J1224+0037	1.482	1.364	$0.68 \pm 0.07$	$17.03^{+0.05}_{-0.04}$	PLLS	STIS
J1224+0037	1.482	1.268	> 2.69	> 17.63	MgII	STIS
B1225+3145	2.219	1.796	> 5.75	> 17.96	R1,R2	FOS-H
J1228+1018	2.305	0.939	> 0.69	> 17.04	MgII	STIS
J1232-0224	1.045	0.832	$1.26 \pm 0.08$	$17.30^{+0.03}_{-0.03}$	21cm	FOS-L
J1232-0224	1.045	0.772	$0.51 \pm 0.09$	$16.92^{+0.07}_{-0.09}$	21cm	FOS-L
J1308+3005	0.803	0.821	$2.93 \pm 0.22$	$17.67^{+0.03}_{-0.03}$	Prox	FOS-L
J1313-2716	2.186	1.684	> 4.34	> 17.84	R1,R2	STIS
J1319+2728	1.014	0.661	$3.08 \pm 0.26$	$17.69^{+0.04}_{-0.04}$	R1,R2	FOS-L
B1320+2925	0.960	0.872	$1.37 \pm 0.12$	$17.34^{+0.04}_{-0.04}$	R1	FOS-L

TABLE 4 — *Continued*

Object <sup>a</sup>	$z_{\text{em}}$	$z_{\text{LLS}}^{\text{b}}$	$\tau_{\text{LLS}}$	$\log N_{\text{HI}}$	Sample <sup>c</sup>	Instrument <sup>d</sup>
J1321+1106	2.181	1.849 <sup>b</sup>	> 2.63	> 17.62	R2	STIS
J1321+2847	1.703	1.135	$2.56 \pm 0.26$	$17.61^{+0.04}_{-0.04}$	R1,R2	FOS-L
J1322+4739	1.554	1.435	$1.27 \pm 0.04$	$17.31^{+0.01}_{-0.02}$	R1	STIS
J1322+4739	1.554	1.078	> 2.44	> 17.59	R1,R2	STIS
B1323+6530	1.618	1.609	> 4.18	> 17.82	Prox	FOS-H
B1329+4117	1.930	1.841	$0.38 \pm 0.03$	$16.78^{+0.04}_{-0.03}$	PLLS	FOS-H
B1329+4117	1.930	1.602	$1.02 \pm 0.04$	$17.21^{+0.02}_{-0.02}$	MgII	FOS-H
B1329+4117	1.930	1.283	> 2.76	> 17.64	MgII	FOS-H
B1334-0033	2.783	2.201	$0.81 \pm 0.03$	$17.12^{+0.01}_{-0.02}$	PLLS	FOS-H
J1341+0059	1.714	1.597	> 3.25	> 17.71	R1,R2	STIS
J1341+4123	1.204	1.063	$0.58 \pm 0.04$	$16.97^{+0.03}_{-0.04}$	PLLS	FOS-L
J1351-0007	1.444	1.159 <sup>b</sup>	> 3.67	> 17.76	R1,R2	FOS-L
J1354+0052	1.121	0.666 <sup>b</sup>	> 3.74	> 17.77	R1,R2	FOS-L
J1404-0130	2.522	1.719	> 3.56	> 17.75	R1,R2	STIS
J1419-0036	0.969	0.823	> 1.32	> 17.32	MgII	STIS
J1420-0054	1.458	1.348	> 3.66	> 17.76	MgII	STIS
J1423+3252	1.905	1.491	$3.46 \pm 0.11$	$17.74^{+0.02}_{-0.01}$	R1,R2	STIS
J1423+3252	1.905	1.176	> 2.09	> 17.52	R2	STIS
J1426+0051	1.333	0.844	> 1.29	> 17.31	MgII	STIS
J1427-1203	0.805	0.652 <sup>b</sup>	> 2.76	> 17.64	R2	FOS-L
J1431-0050	1.188	0.858	> 1.51	> 17.38	LQ	STIS
B1435+6349	2.068	1.938	$1.88 \pm 0.07$	$17.48^{+0.01}_{-0.02}$	R1	FOS-H
B1435+6349	2.068	1.925	> 3.03	> 17.68	LQ	FOS-H
J1436-0051	1.273	1.264	$0.98 \pm 0.06$	$17.20^{+0.02}_{-0.03}$	PLLS	STIS
J1436-0051	1.273	0.930	> 1.78	> 17.45	MgII	STIS
J1455-0045	1.375	1.095	> 3.12	> 17.69	MgII	STIS
J1501+0019	1.930	1.486	> 3.50	> 17.74	MgII	STIS
J1513+1011	1.546	1.042 <sup>b</sup>	> 3.71	> 17.77	R1,R2	FOS-L
B1517+2356	1.903	1.887	$0.53 \pm 0.03$	$16.93^{+0.02}_{-0.02}$	PLLS	FOS-H
B1517+2356	1.903	1.725	$1.95 \pm 0.09$	$17.49^{+0.02}_{-0.01}$	R1	FOS-H
J1521-0009	1.318	0.961	> 1.92	> 17.48	MgII	STIS
J1525+0026	0.801	0.797	> 1.33	> 17.33	Prox	STIS
J1537+0021	1.754	1.647	> 3.41	> 17.73	MgII	STIS
J1537+3358	1.025	0.915	> 3.03	> 17.68	DLA	STIS
J1539+4735	0.772	0.730	$1.21 \pm 0.10$	$17.29^{+0.03}_{-0.04}$	R1	FOS-L
J1601+1714	1.952	1.581	$1.87 \pm 0.27$	$17.48^{+0.06}_{-0.07}$	R1	FOS-L
J1614+4704	1.860	1.867	$0.47 \pm 0.04$	$16.87^{+0.04}_{-0.03}$	Prox,PLLS	STIS
J1614+4704	1.860	1.735	$0.54 \pm 0.05$	$16.93^{+0.04}_{-0.04}$	PLLS	STIS
J1614+4704	1.860	1.411	> 3.98	> 17.80	R1,R2	STIS
B1622+2352	0.927	0.891	> 2.24	> 17.55	MgII	FOS-H
J1623+2653	2.526	1.042	> 3.08	> 17.69	R1,R2	FOS-L
J1629+3808	1.461	1.110	$1.60 \pm 0.09$	$17.41^{+0.03}_{-0.02}$	R1	FOS-L
B1630+3744	1.478	1.096	$0.29 \pm 0.04$	$16.66^{+0.05}_{-0.06}$	PLLS,IUE	FOS-H
J1631+1156	1.792	0.902	> 1.51	> 17.38	MgII	STIS
J1637+2509	1.110	0.894	> 1.56	> 17.39	DLA	STIS
J1649+3046	1.123	1.078	> 3.41	> 17.73	R1,R2	STIS
J1701+6412	2.722	2.293	$0.31 \pm 0.05$	$16.69^{+0.07}_{-0.08}$	PLLS,IUE	STIS
J1701+6412	2.722	2.160	$0.51 \pm 0.05$	$16.92^{+0.04}_{-0.05}$	PLLS,IUE	STIS
J1701+6412	2.722	1.846	$0.39 \pm 0.06$	$16.80^{+0.06}_{-0.07}$	PLLS,IUE	STIS
J1701+6412	2.722	1.725	$0.56 \pm 0.07$	$16.95^{+0.05}_{-0.06}$	PLLS,IUE	STIS
J1704+7057	2.015	1.810	$2.60 \pm 0.13$	$17.62^{+0.02}_{-0.02}$	R1,R2	STIS
J1704+7057	2.015	1.101 <sup>b</sup>	> 2.31	> 17.56	R2	STIS
J1712+5559	1.358	1.209	> 3.00	> 17.68	MgII	STIS
B1715+5331	1.940	1.633	$0.64 \pm 0.03$	$17.01^{+0.02}_{-0.02}$	PLLS	FOS-H
J1727+5302	1.444	1.032	> 2.49	> 17.60	MgII	STIS
J1727+5302	1.444	0.948	.....	.....	MgII,Blue	STIS
J1729+5758	1.342	1.130	$0.35 \pm 0.04$	$16.74^{+0.05}_{-0.05}$	PLLS	STIS
J1733+5533	1.072	1.000	> 3.29	> 17.72	MgII	STIS
J1736+5938	1.410	1.400	> 3.50	> 17.74	Prox	STIS
B1821+1042	1.360	1.252	> 3.27	> 17.71	MgII	FOS-H
J1858+5645	1.595	1.235	> 3.65	> 17.76	MgII	STIS
J2051+1950	2.367	1.747 <sup>b</sup>	> 2.96	> 17.67	R2	STIS
J2144-0754	1.811	1.802	> 3.55	> 17.75	Prox	STIS
J2151+2130	1.534	1.004	> 1.87	> 17.47	MgII	STIS
J2151+2130	1.534	0.915	.....	.....	MgII,Blue	STIS
J2215-2944	2.706	1.954	$1.77 \pm 0.06$	$17.45^{+0.02}_{-0.01}$	R1	STIS
J2215-2944	2.706	1.900	$0.44 \pm 0.08$	$16.85^{+0.07}_{-0.09}$	PLLS	STIS
J2215-2944	2.706	1.610	$0.62 \pm 0.09$	$16.99^{+0.06}_{-0.06}$	PLLS	STIS

TABLE 4 — *Continued*

Object <sup>a</sup>	$z_{\text{em}}$	$z_{\text{LLS}}^{\text{b}}$	$\tau_{\text{LLS}}$	$\log N_{\text{HI}}$	Sample <sup>c</sup>	Instrument <sup>d</sup>
J2233-6033	2.238	1.929	$1.53 \pm 0.03$	$17.39^{+0.01}_{-0.01}$	R1	STIS
J2233-6033	2.238	1.872	$0.48 \pm 0.03$	$16.88^{+0.03}_{-0.02}$	PLLS	STIS
J2331+0038	1.486	1.143	$> 3.77$	$> 17.78$	MgII	STIS
J2339-0029	1.340	0.967	$> 1.98$	$> 17.50$	MgII	STIS
J2352-0028	1.624	1.245	$> 2.62$	$> 17.62$	MgII	STIS

<sup>a</sup> Objects with a B preface designate objects listed with coordinates from the Besselian epoch (1950). These objects were observed with the FOS high resolution gratings and can be found in Bechtold et al. (2002). Objects with a J preface designate objects listed with coordinates from the Julian epoch (2000). These objects were observed with either the FOS low resolution gratings or the STIS low resolution gratings described in § 3 and listed in Table 1 and Table 2.

<sup>b</sup> Redshifts marked b indicate the break of the Lyman limit was used to determine the redshift of the absorber. Unmarked redshifts indicate the Lyman series lines were used to determine the redshift of the absorber.

<sup>c</sup> The sample (R1 or R2) where a LLS was discovered. An absorber is marked R1 if  $z_{\text{LLS}} \geq z_{\text{min}}$  for that object and  $\tau_{\text{LLS}} \geq 1$ . An absorber is marked R2 if  $z_{\text{LLS}} \geq z_{\text{min}}$  for that object and

$\tau_{\text{LLS}} \geq 2$ . The rest of the designations indicate why an absorber was not included in the statistical analysis. Blue, the redshift of the absorber is blueward of  $z_{\text{min}}$  for that object; DLA, a known DLA prior to observation; GL, part of a gravitationally lensed system (for these systems, we did not include any absorbers associated with the lensing object); MgII, known strong Mg II system prior to observation; PLLS,  $\tau_{\text{LLS}} < 1$ ; LQ,  $z_{\text{LLS}} < z_{\text{min}}$  for that object (this occurred in systems where we could identify the Lyman series of a system, but the break occurred outside of our established acceptable redshift path); IUE, objects previously observed with IUE (these objects were targeted with *HST* because of their strong UV flux as measured from IUE observations); 21 cm, known strong 21 cm system prior to observation; and finally, Prox, absorbers where  $z_{\text{LLS}} \leq 3000 \text{ km s}^{-1}$  from  $z_{\text{em}}$ .

<sup>d</sup> The instrument used to observe the object (see § 3).

TABLE 5  
REDSHIFT DENSITY OF LLSs FOR R1 AND R2.

z	$\Delta X$	$\Delta z$	N	$\langle z_{\text{LLS}} \rangle$	$l(z)$	$l(X)$	$\Delta r_{\text{LLS}} (\text{h}_{70}^{-1} \text{ Mpc})$
$\tau_{\text{LLS}} \geq 1$							
[0.255, 2.594]	195.73	79.23	61	1.434	$0.77 \pm 0.11$	$0.31 \pm 0.04$	.....
[0.255, 1.060]	59.13	29.54	15	0.785	$0.51 \pm 0.14$	$0.25 \pm 0.07$	3047
[1.060, 1.423]	48.54	19.56	16	1.194	$0.82 \pm 0.22$	$0.33 \pm 0.09$	1213
[1.423, 1.824]	45.63	16.47	15	1.613	$0.91 \pm 0.25$	$0.33 \pm 0.09$	731
[1.824, 2.594]	42.44	13.66	15	2.142	$1.10 \pm 0.32$	$0.35 \pm 0.10$	392
$\tau_{\text{LLS}} \geq 2$							
[0.242, 2.594]	234.70	96.14	50	1.515	$0.52 \pm 0.08$	$0.21 \pm 0.03$	.....
[0.242, 1.078]	80.38	40.03	15	0.895	$0.37 \pm 0.10$	$0.19 \pm 0.05$	3645
[1.078, 1.544]	73.50	29.03	15	1.157	$0.52 \pm 0.14$	$0.20 \pm 0.05$	1995
[1.544, 1.947]	44.28	15.52	10	1.751	$0.64 \pm 0.21$	$0.23 \pm 0.08$	917
[1.947, 2.594]	36.54	11.56	10	2.257	$0.86 \pm 0.30$	$0.27 \pm 0.09$	457

TABLE 6  
PARAMETERS OF  $l(z) = l_0(1+z)^\gamma$ .

Paper	$\tau_{\text{LLS}} \geq$	$z$	$l_0^{\text{a}}$	$\gamma$
Sargent et al. 1989	1	[0.6, 3.6]	0.76	$0.68 \pm 0.54$
Lanzetta 1991	1	[0.35, 2.5]	1.2	$0.3 \pm 0.9$
Storrie-Lombardi et al. 1994	1	[0.4, 4.7]	0.27	$1.55 \pm 0.45$
Stengler-Larrea et al. 1995	1	[0.3, 4.2]	0.25	$1.5 \pm 0.39$
This Paper	1	[0.25, 2.59]	0.28 <sup>a</sup>	$1.19 \pm 0.56$
Prochaska et al. 2010	2	[3.5, 4.4]	0.0006 <sup>a</sup>	$5.2 \pm 1.5$
This Paper	2	[0.24, 2.59]	0.17 <sup>a</sup>	$1.33 \pm 0.61$
This Paper	2	[0.24, 4.9]	0.30 <sup>a</sup>	$1.83 \pm 0.21$

<sup>a</sup>  $l_0 = l_*(1+z_*)^{-\gamma}$

TABLE 7  
REDSHIFT DENSITY OF LLSs FOR RP10.

z	$\Delta X$	$\Delta z$	N	$\langle z_{\text{LLS}} \rangle$	$l(z)$	$l(X)$	$\Delta r_{\text{LLS}} (\text{h}_{70}^{-1} \text{ Mpc})$
[0.242, 1.078]	80.38	40.03	15	0.895	$0.37 \pm 0.10$	$0.19 \pm 0.05$	3645
[1.078, 1.544]	73.50	29.03	15	1.157	$0.52 \pm 0.14$	$0.20 \pm 0.05$	1995
[1.544, 1.947]	44.28	15.52	10	1.751	$0.64 \pm 0.21$	$0.23 \pm 0.08$	917
[1.947, 2.594]	36.54	11.56	10	2.257	$0.86 \pm 0.30$	$0.27 \pm 0.09$	457
[3.500, 3.663]	119.91	31.07	56	3.593	$1.80 \pm 0.26$	$0.47 \pm 0.07$	94
[3.663, 3.925]	109.00	27.62	55	3.799	$1.99 \pm 0.29$	$0.50 \pm 0.07$	77
[3.925, 4.907]	71.98	17.50	45	4.125	$2.57 \pm 0.44$	$0.63 \pm 0.11$	50